



OPEN ACCESS

EDITED BY
Fan Yang,
Lanzhou University, China

REVIEWED BY
Fan Huang,
CAGS, China
Xingyuan Li,
Lanzhou University, China
Qian Liu,
Northwest University, China

*CORRESPONDENCE
Da Zhang,
✉ zhangda@cugb.edu.cn

SPECIALTY SECTION
This article was submitted to
Geochemistry,
a section of the journal
Frontiers in Earth Science

RECEIVED 31 October 2022
ACCEPTED 13 January 2023
PUBLISHED 02 February 2023

CITATION
Hu B, Zhang D, Zhang X, Zhang Z, Wang S
and Hu J (2023), Identification of Baihesi
aluminous A-type granite: Magmatic
response to the onset of Cretaceous
extension in eastern Jiangnan Massif,
South China.
Front. Earth Sci. 11:1085767.
doi: 10.3389/feart.2023.1085767

COPYRIGHT
© 2023 Hu, Zhang, Zhang, Zhang, Wang
and Hu. This is an open-access article
distributed under the terms of the [Creative Commons Attribution License \(CC BY\)](https://creativecommons.org/licenses/by/4.0/).
The use, distribution or reproduction in
other forums is permitted, provided the
original author(s) and the copyright
owner(s) are credited and that the original
publication in this journal is cited, in
accordance with accepted academic
practice. No use, distribution or
reproduction is permitted which does not
comply with these terms.

Identification of Baihesi aluminous A-type granite: Magmatic response to the onset of Cretaceous extension in eastern Jiangnan Massif, South China

Bojie Hu¹, Da Zhang^{1*}, Xinming Zhang¹, Zhihui Zhang²,
Sen Wang^{3,4,5} and Jiaxiu Hu¹

¹School of Earth Sciences and Resources, China University of Geosciences (Beijing), Beijing, China, ²Development and Research Center, China Geological Survey, Beijing, China, ³Institute of Geomechanics, Chinese Academy of Geological Sciences, Beijing, China, ⁴Key Laboratory of Paleomagnetism and Tectonic Reconstruction, Ministry of Natural Resources, Beijing, China, ⁵Research Center of Polar Geosciences, China Geological Survey, Beijing, China

The Cretaceous lithospheric extension in South China is very distinct and expressed by systematic extension-related geological records which are concentrated in the coastal terrane, Shi-Hang Rift, and Jiangnan Massif. The Cretaceous extension in the coastal terrane and Shi-Hang Rift began almost simultaneously during 145–140 Ma, while there is a lack of reliable magmatic indication for tectonic extension in the Jiangnan Massif during 145–140 Ma. This paper reports a newly discovered Baihesi granite with a concordant age of 142.52 ± 0.57 Ma (MSWD = 1.2) on the southeast margin of the eastern Jiangnan Massif with evidence from petrology, geochronology, petrochemistry and Hf isotopes. The Baihesi granite is a monzogranite and classified as a peraluminous, high-K calc-alkaline series. The trace element compositions are characterized by relatively flat rare earth element patterns; strong depletion of Eu; slightly enriched light rare earth elements; enrichment of Cs, Rb, Th, U, and Pb; and depletion of Ba, Sr, P, and Ti. Combined with other petrochemistry characteristics, such as high SiO₂ content, high differentiation index, low Zr/Hf and Nb/Ta ratios, low ratio between light and heavy REEs, low P₂O₅ content, and high zirconium saturation temperature, Baihesi granite is proven to be highly evolved aluminous A-type granite. The $\epsilon_{\text{Hf}}(t)$ values of Baihesi granite range from –5.57 to –2.37, with two-stage model ages (T_{DM2}) ranging from 1,551 to 1,345 Ma, suggesting a similar source to Neoproterozoic arc-related magmatic rocks in the Shuangqiaoshan Group. We argue that Baihesi granite has originated mainly from partial melting of a reworked juvenile crust related to Neoproterozoic arc-related magmatism in the Jiangnan Massif, which was controlled by subduction along the South China active continental margin. Furthermore, we constrain the onset of Cretaceous extension in the eastern Jiangnan Massif to be 145–140 Ma and highlight the Early Cretaceous reactivation of the northeastern Jiangxi Province fault zone and the structural inheritance in intraplate tectonics.

KEYWORDS

Cretaceous lithospheric extension, South China, Baihesi granite, eastern Jiangnan Massif, highly evolved aluminous A-type granite

1 Introduction

The Cretaceous lithospheric extension in South China, even in entire eastern Eurasia, is very remarkable and typical (Chu et al., 2019; Li et al., 2014; Liu et al., 2021). Systematic extension-related geological records, including bimodal volcanic rocks, mafic dikes, A-type granitoids, half-grabens, faulted basins, and low-angle detachment faults, indicate that a long-term extensional regime has dominated the South China Block during the Cretaceous (Chu et al., 2019; Li et al., 2014). As to spatial distribution, these geological records are obviously concentrated in two regions, namely, the coastal terrane (CT) and the intraplate ancient suture zone-related terranes in South China (Figure 1). Many previous studies have been conducted on these records to understand the temporal and spatial evolution of South China during the Cretaceous (e.g., Chu et al., 2019; Ji et al., 2018a, 2018b; Jiang et al., 2015; Li et al., 2013; Lin et al., 2000; Shu et al., 2009; Yu et al., 2006; Zhou and Li, 2000; Zhou et al., 2006). Among these studies, the research of magmatism, which can be used as the “litho-probe” or “window” to help understand the Earth’s interior and tectonic evolution, played an important role in constraining the temporal stages and dynamic mechanism of the Cretaceous extension (Mo, 2019).

The Cretaceous magmatism in the CT developed from the earliest Cretaceous to the early Late Cretaceous (140–90 Ma, Zhou et al., 2006), including the felsic volcanic rocks from the eastern Guangdong and Fujian provinces with an early stage of 143–130 Ma (Guo et al., 2012), and the volcanic rocks from the southeastern Zhejiang Province with an early stage of 145–129 Ma or 140–128 Ma (Li et al., 2014; Liu et al., 2012). According to the different output characteristics of the extension-related geological records, the intraplate ancient suture zone-related terranes can be subdivided into the Shi-Hang Rift (SR) and Jiangnan Massif (JM). In the northwestern Zhejiang Province, which is located in the most northeast segment of the SR and closest to the CT, the volcanic activity related to extension began at ca.140 Ma (Liu et al., 2014), and A-type granites formed during 136–126 Ma (Wong et al., 2009; Yang et al., 2012). In the Xiangshan region, which is located in the middle segment of the SR and hundreds of kilometers away from the coast, extension-related volcanism and A-type granites occurred between 137 and 135 Ma (Yang et al., 2011). Hence, magmatism related to the Cretaceous extension in the CT and SR began almost simultaneously during 145–140 Ma.

However, in the eastern Jiangnan Massif (EJM), the magmatism related to the Cretaceous extension mainly occurred between 134 Ma

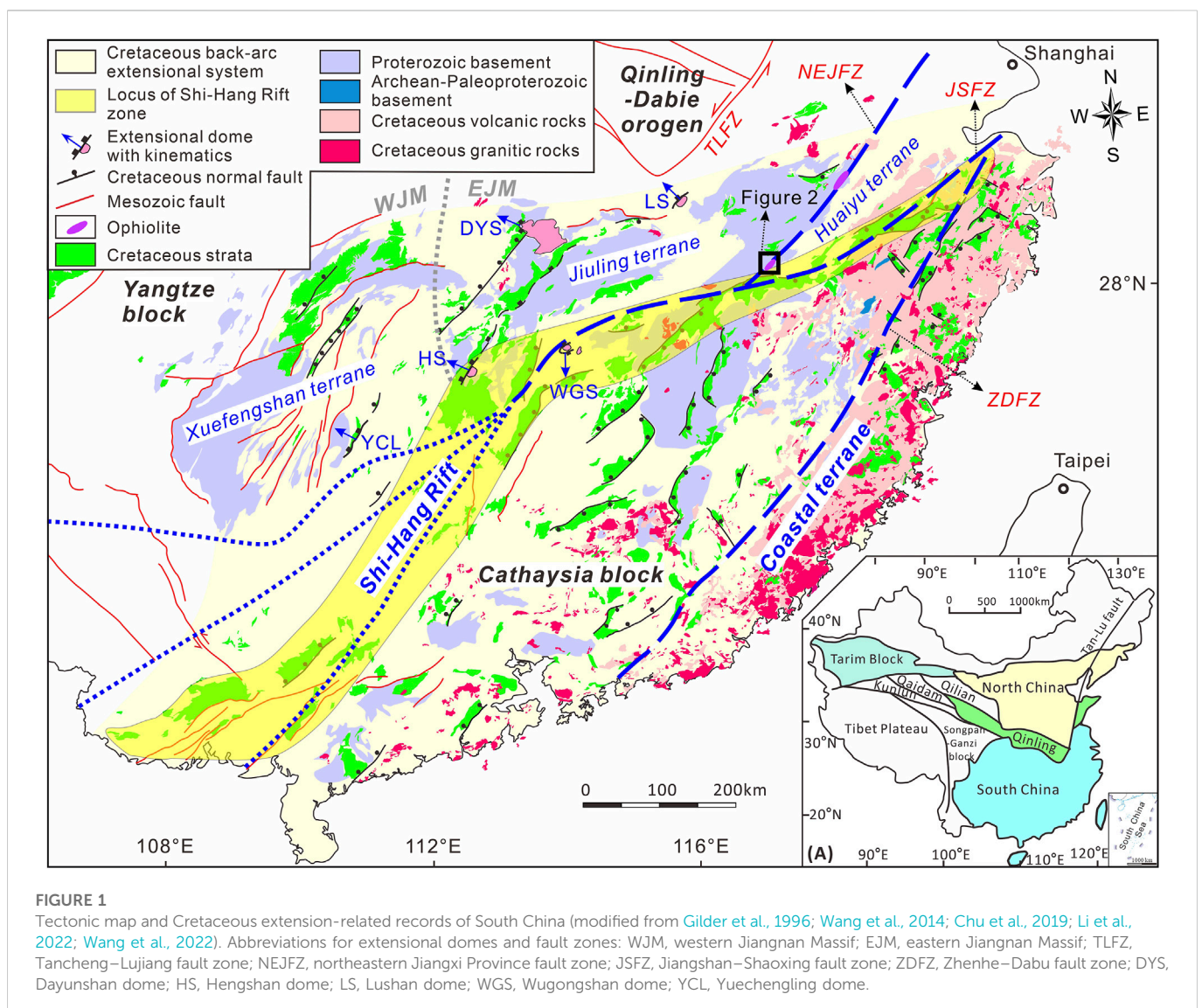


TABLE 1 Early Cretaceous granitoids related to lithospheric extension in the EJM.

Location	Lithology	Type of granite	Age (mineral, methods)	Source
Xianglushan	Biotite granite	S	123.81 ± 0.77 Ma (zircon, LA-ICPMS)	Dai et al. (2018)
Dongping	Biotite granite	S	132.9 ± 1.4 Ma (zircon, LA-ICPMS)	Hu et al. (2018)
Pengshan	Granite	I	128 ± 1 Ma (zircon, SHRMP)	Luo et al. (2010)
Maogongdong (Dahutang)	Porphyritic granite		132.5 ± 1.8 Ma (zircon, LA-ICPMS)	Chen et al. (2018)
Yunshan	Topaz-bearing muscovite monzogranite		129.4 ± 0.2 Ma (zircon, LA-ICPMS)	Yang et al. (2021)
	Two-mica monzogranite		130.6 ± 0.2 Ma (zircon, LA-ICPMS)	
	Granophyre		129.7 ± 0.2 Ma (zircon, LA-ICPMS)	
Ehu	Two-mica granites	S	121.7 ± 2.9 Ma (zircon, LA-ICPMS)	Jiang et al. (2011)
	Two-mica monzogranite		132.0 ± 0.6 Ma (zircon, LA-ICPMS)	Qiu and Qiu, (2016)
Zhenzhushan	Granite porphyry	A	133.7 ± 0.2 Ma (zircon, LA-ICPMS)	Yang et al. (2021)

and 121 Ma (Table 1), including Xianglushan (Dai et al., 2018), Dongping (Hu et al., 2018), Pengshan (Luo et al., 2010), Yunshan (Yang et al., 2021), Ehu (Jiang et al., 2011; Yang et al., 2021), and Zhenzhushan (Yang et al., 2021). Furthermore, another significant stage of magmatism developed in the EJM mainly during 154–136 Ma (He et al., 2022; Yang et al., 2021; Zhang et al., 2020). It is controversial whether the tectonic setting of 154–136 Ma magmatism in the EJM was lithospheric extension or compression (Huang and Jiang, 2014; Mao et al., 2017; Pan et al., 2018) and has been interpreted as a compression–extension transition (Feng et al., 2018).

It follows that, being different from the coastal zone and the Shi-Hang Zone, the tectonic setting of the EJM in the earliest Cretaceous is not well-constrained. This problem is mainly attributed to the absence of magmatic record, such as bimodal volcanic rocks and A-type granitoids, which could provide explicit evidence for the extensional tectonic setting. The manifestation of extension is attenuated from the coast to the inland regions, which was characterized by less volcanic activity in extensional basins and weaker crust–mantle interaction in magmatism. In this case, A-type granite provides a rare and relatively reliable indicator for recognizing the tectonic extension in the inland region because A-type granites commonly occur in post-orogenic or intraplate extensional tectonic settings (Eby, 1992; Eby and Kochhar, 1990; Whalen et al., 1987).

In this contribution, we report a newly discovered A-type granite with a concordant age of 142.52 ± 0.57 Ma (MSWD = 1.2) on the southeast margin of the EJM, shedding light on the fact that the Cretaceous lithospheric extension has started as early as ca. 145–140 Ma in the EJM.

2 Geological setting

The Jiangnan Massif (JM), spanning the central part of the South China Block (SCB) and separating the Yangtze Block in the northwest and the Cathaysia Block in the southeast (Figure 1; Zhao and Cawood, 2012), is an ENE-trending and ca. 1,500-km-long tectonic belt consisting of Neoproterozoic undeformed granitoids and low-greenschist facies metamorphosed sedimentary rocks (Wang et al., 2008; Wang et al., 2013; Wang et al., 2014; Yao et al., 2019). Meanwhile, the JM was divided into the Huaiyu terrane (HYT),

Jiuling terrane (JLT), and Southeast terrane (ST) from east to west (Figure 1; Wang et al., 2022; Yao et al., 2019). The northeastern Jiangxi Province fault zone (NEJFZ), considered to be the boundary structure between the JLT and HYT, is the most outstanding suture zone for Neoproterozoic Jiangnan orogenesis, in which there is the most systematic evidence including ophiolite, high-pressure metamorphic rock, syn-orogenic granite, and post-orogenic granite (Li et al., 2009; Shu et al., 1994; Wang et al., 2008; Wang et al., 2014; Yao et al., 2012; Ye et al., 2007). The JM originated from the collisional welding of the Yangtze Block and Cathaysia Block during Neoproterozoic (Charvet, 2013; Yao et al., 2019; Zhao and Cawood, 2012) and was strongly modified by intraplate compressional deformation during the Early Paleozoic and Early Mesozoic, so it was also a typical multiphase intraplate orogen (Chu and Lin, 2014; Chu et al., 2015; Li et al., 2016; Shu, 2021).

The Baihesi granite (BMSG), located on the southeastern margin of the JM, is adjacent to the NEJFZ on the southeast. The strata, structures, and magmatic rocks in the study area are controlled by the NNE-trending NEJFZ. The sedimentary strata consist of Neoproterozoic Shuangqiaoshan Group metasedimentary rocks, Carboniferous carbonates, Triassic clastic rocks, Jurassic clastic rocks, and Quaternary sediments. NNE- and NNW-striking faults are developed in the Fuquanshan area where BMSG is located, with dominant NNE-striking. The Fuquanshan anticline is the major fold in the study area. It is cored by Neoproterozoic strata and flanked by Carboniferous to Jurassic strata (Figure 2). Magmatic rocks are widespread in the study area, including the Fuquanshan granitic pluton (FQSG) that intruded in the core of the Fuquanshan anticline and a series of NNE-trending granitic dikes located the southwest of FQSG, namely, BMSG. FQSG intruded in Neoproterozoic metasedimentary rocks and Carboniferous carbonate as a batholith. BMSG intruded along the interlayer structures of the Neoproterozoic metasedimentary rocks with several sub-parallel sheets (Figure 3).

3 Sampling and analytical methods

To ensure the representativeness of the samples, we selected several fresh samples of BMSG from different parts of the outcrop during the

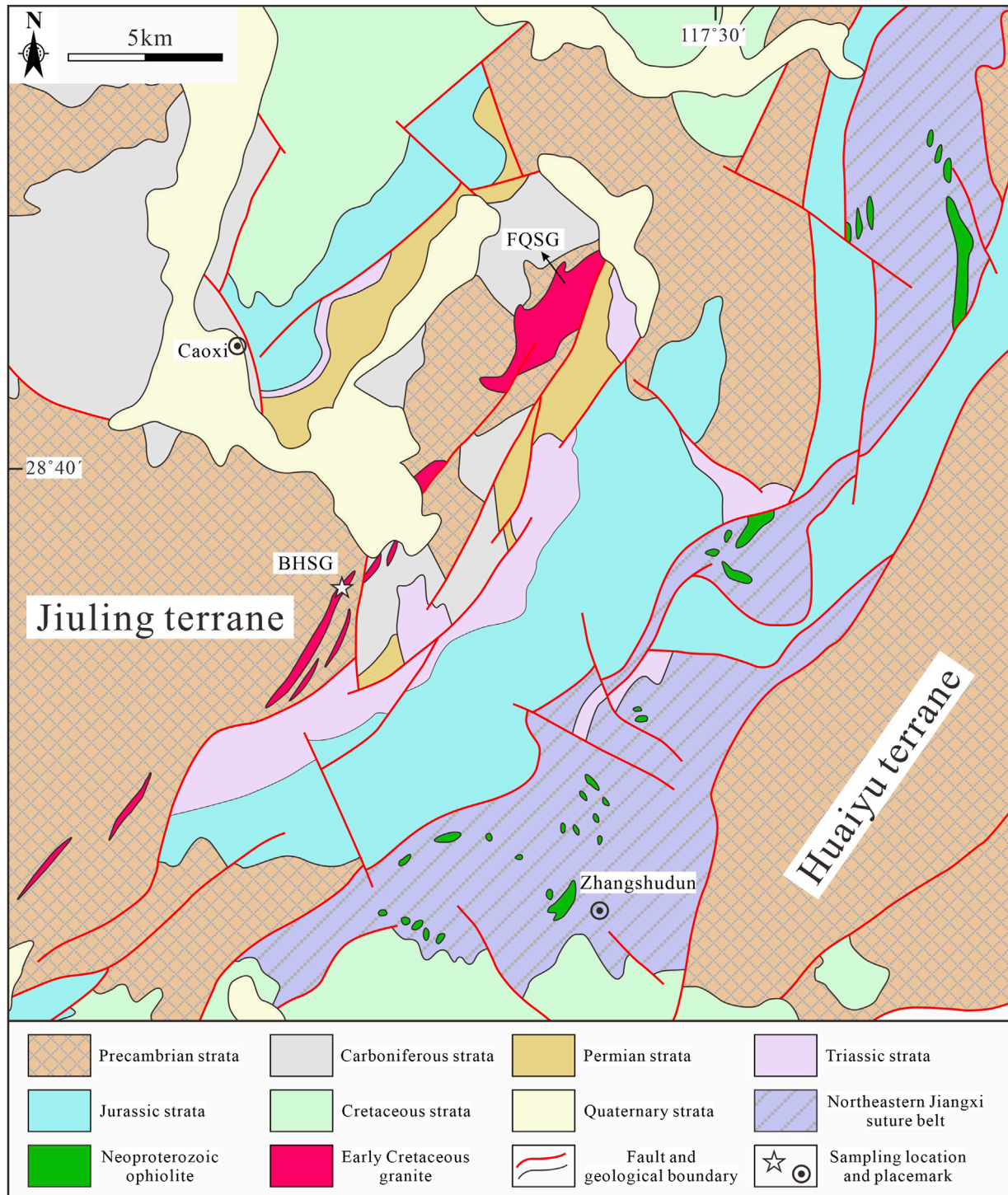


FIGURE 2

Geological map of the Fuquanshan area (modified from Northeastern Jiangxi Geological Party, Bureau of Geology and Mineral Resources of Jiangxi Province).

fieldwork. BHSG shows porphyritic textures with phenocrysts of feldspar and quartz (Figures 4A–C) and is primarily composed of quartz (35%), plagioclase (30%), K-feldspar (30%), and biotite (5%), as well as minor accessory minerals such as zircon (Figures 4A–H). The corrosion of quartz phenocryst is obvious (Figure 4C). The alteration of both types of feldspar is obvious, but the crystalline form and crystal

twin can be observed (Figures 4D–G). The sericitization of plagioclase is obvious, and it can be identified according to the polysynthetic twin (Figures 4D, F). The K-feldspar suffered obvious argillation and carbonation, and it can be identified according to the Carlsbad twin (Figures 4E, F). The alteration of biotite is weak (Figure 4H). Five samples of BHSG were analyzed for whole-rock major and trace

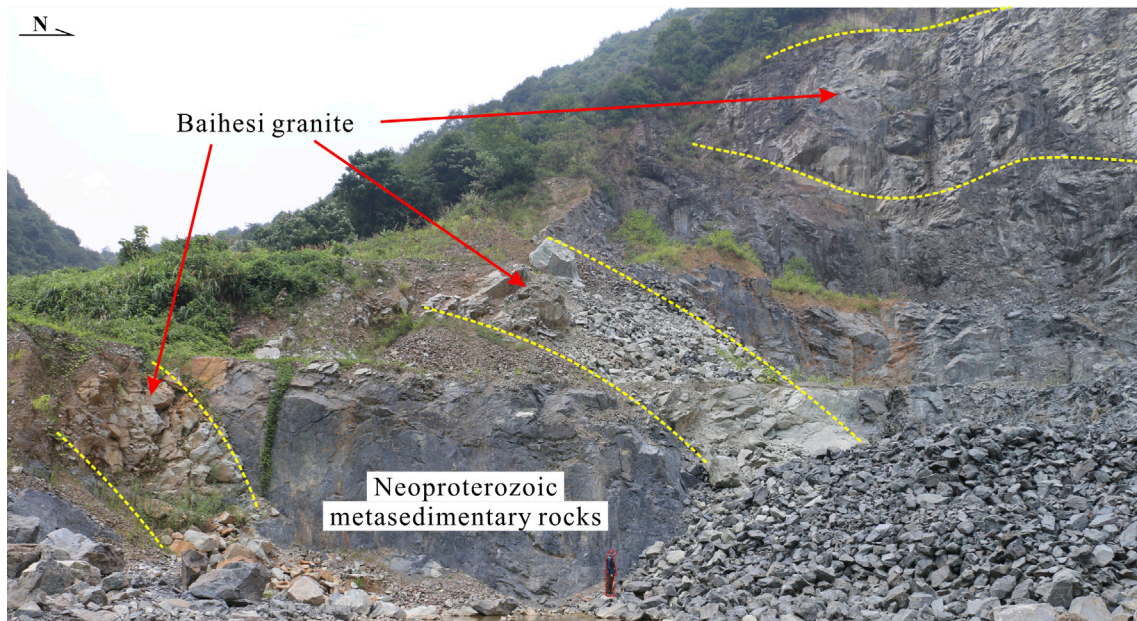


FIGURE 3
Field photo showing the emplacement characteristic of BHSg.

element composition. One of those was analyzed for zircon U–Pb dating, trace element composition, and Hf isotopes.

3.1 U–Pb dating and Hf isotope analysis of zircons

Zircon grains were separated from the samples by conventional heavy liquid and magnetic separation techniques. Transmission and reflected light and cathodoluminescence images (CL) were taken to select optimum laser ablation targets. U–Pb dating and trace element analysis of zircon were performed on an Agilent 7900 ICP-MS instrument using a GeolasPro laser ablation system. Detailed operating conditions for the laser ablation system and the ICP-MS instrument are the same as described by Zong et al. (2017). Zircon GJ-1 and NIST610 were used as an external standard for U–Pb dating and trace element calibration. The concordia age of the GJ-1 sample obtained in this experiment is 601.8 ± 1.3 Ma (MSWD = 0.27), which is consistent with the reference value (TIMS $^{206}\text{Pb}/^{238}\text{U}$ age = 599.8 ± 4.5 Ma; Jackson et al., 2004). Data processing was performed using ICPMSDataCal software (Liu et al., 2010). IsoplotR (Vermeesch, 2018) was used to calculate the weighted mean age and draw the concordant diagram. After completing the zircon U–Pb isotopic analysis mentioned previously, *in situ* Hf isotopic analysis was performed on the tested zircons. The experiments were performed on a multiple receiver plasma mass spectrometer (MC-ICP-MS). Laser ablation conditions were $10 \text{ J}/\text{cm}^2$ of laser energy, 8 Hz of ablation frequency, and $44 \mu\text{m}$ of spot diameter. Zircon Plesovice was used as the reference standard, yielding an average $^{176}\text{Hf}/^{177}\text{Hf}$ value of 0.2824780 ± 0.0000034 in this study, which is consistent with the reference value (0.282482 ± 0.000013 ; Sláma et al., 2008). The aforementioned analyses were performed at the Wuhan Sample Solution Analytical Technology Co., Ltd., Wuhan, China.

3.2 Whole rock major- and trace-element analyses

The whole rock major- and trace-element analyses were performed at the Wuhan Sample Solution Analytical Technology Co., Ltd., Wuhan, China. The sample pretreatment of whole rock major-element analysis was performed by the melting method. A mixture of lithium tetraborate, lithium metaborate, and lithium fluoride, with a mixing ratio of 45:10:5, respectively, was used as a flux. Ammonium nitrate and lithium bromide were used as the oxidant and release agent, respectively. The melting temperature was $1,050^\circ\text{C}$, and the melting time was 15 min. Whole-rock major element analysis was performed using a Zsx Primus II wavelength dispersive X-ray fluorescence spectrometer (XRF) produced by Rigaku, Japan. The test conditions are 50 kV of voltage and 60 mA of current.

The whole-rock trace-element analysis was conducted on an Agilent 7700e ICP-MS. The detailed digestion procedure is as follows: 1) sample powder (200 mesh) was placed in an oven at 105°C for 12-h drying; 2) 50 mg sample powder was accurately weighed and placed in a Teflon bomb; 3) 1 mL HNO_3 and 1 mL HF were slowly added into the Teflon bomb; 4) the Teflon bomb was put in a stainless steel pressure jacket and heated to 190°C in an oven for more than 24 h; 5) after cooling, the Teflon bomb was opened and placed on a hotplate at 140°C and evaporated to incipient dryness, and then 1 mL HNO_3 was added and evaporated to dryness again; 6) 1 mL of HNO_3 , 1 mL of MQ water, and 1 mL internal standard solution of 1 ppm were added, and the Teflon bomb was resealed and placed in the oven at 190°C for more than 12 h; 7) the final solution was transferred to a polyethylene bottle and diluted to 100 g by the addition of 2% HNO_3 .

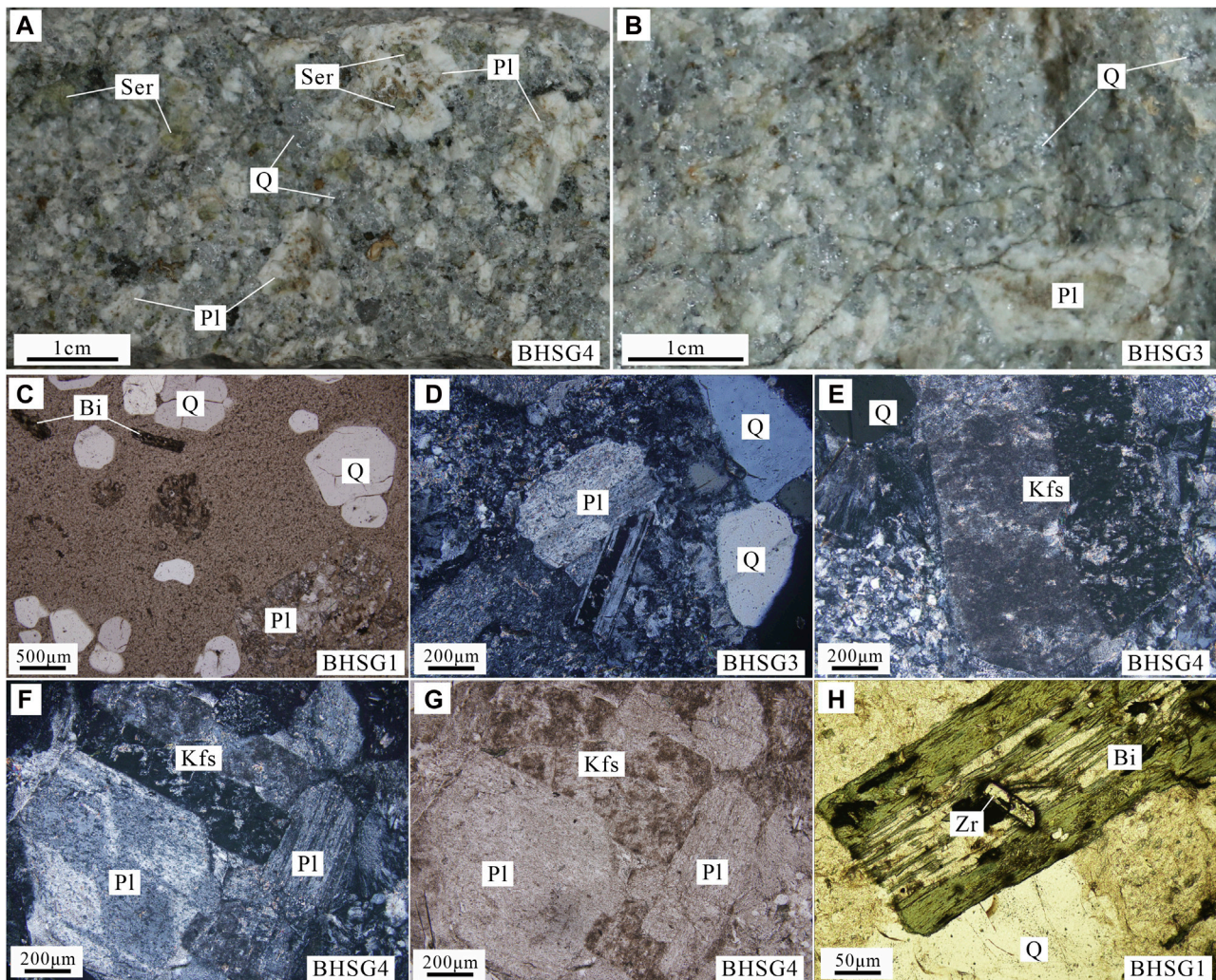


FIGURE 4

Hand specimens (A,B) and microscope photographs (C–H) of BHSB. Abbreviations: Bi, biotite; Kfs, K-feldspar; Pl, plagioclase; Q, quartz; Ser, sericite; Zr, zircon.

4 Results

4.1 CL image and U–Pb age of zircon

These zircons from BHSB are short or long columnar, oscillatory zoned, and dark in the CL image (Figure 5). The Th/U values of zircons from BHSB vary from 0.26 to 0.82 with an average of 0.42. The BHSB data are mainly on the concordant line, presenting a concordant age of 142.52 ± 0.57 Ma (MSWD = 1.2) with a weighted mean age of 142.52 ± 0.92 Ma (MSWD = 2.6) for BHSB (Figure 5). The specific data and calculated parameters are shown in Table 2 and Table 3.

BHSB zircons have some typical features of magmatic zircons, such as morphology, obvious oscillatory zoning, and a relatively high Th/U ratio. Compared with common magmatic zircon, these zircons show darker colors in CL images and have significantly higher Th and U contents (Hoskin, 2005). Petrographic observation provides evidence that some zircons crystallized simultaneously with phenocrysts (Figure 4H). Combining the similar features of petrography, zircon morphology, obvious oscillatory zoning, high Th/U ratio, and indistinguishable

$^{206}\text{Pb}/^{238}\text{U}$ ages, these zircons are classified as magmatic zircons. Therefore, the obtained zircon U–Pb ages of 142.52 ± 0.57 Ma (MSWD = 1.2) for BHSB can represent the crystallization age of magma.

4.2 Zircon Hf isotopic composition

These zircons from BHSB have calculated $(^{176}\text{Hf}/^{177}\text{Hf})_i$ values ranging from 0.282525 to 0.282618 (mean = 0.282573), $\epsilon_{\text{Hf}}(t)$ values ranging from -5.57 to -2.37 (mean = -3.91), and two-stage model ages ($T_{\text{DM}2}$) ranging from 1,551 to 1,345 Ma (mean = 1,444 Ma). The two-stage model ages were calculated using the $^{206}\text{Pb}/^{238}\text{U}$ age of each zircon. The specific data are shown in Table 4.

4.3 Whole-rock chemistry compositions

The analysis results of major elements, trace elements, and the calculated parameters are shown in Table 5 and Table 6.

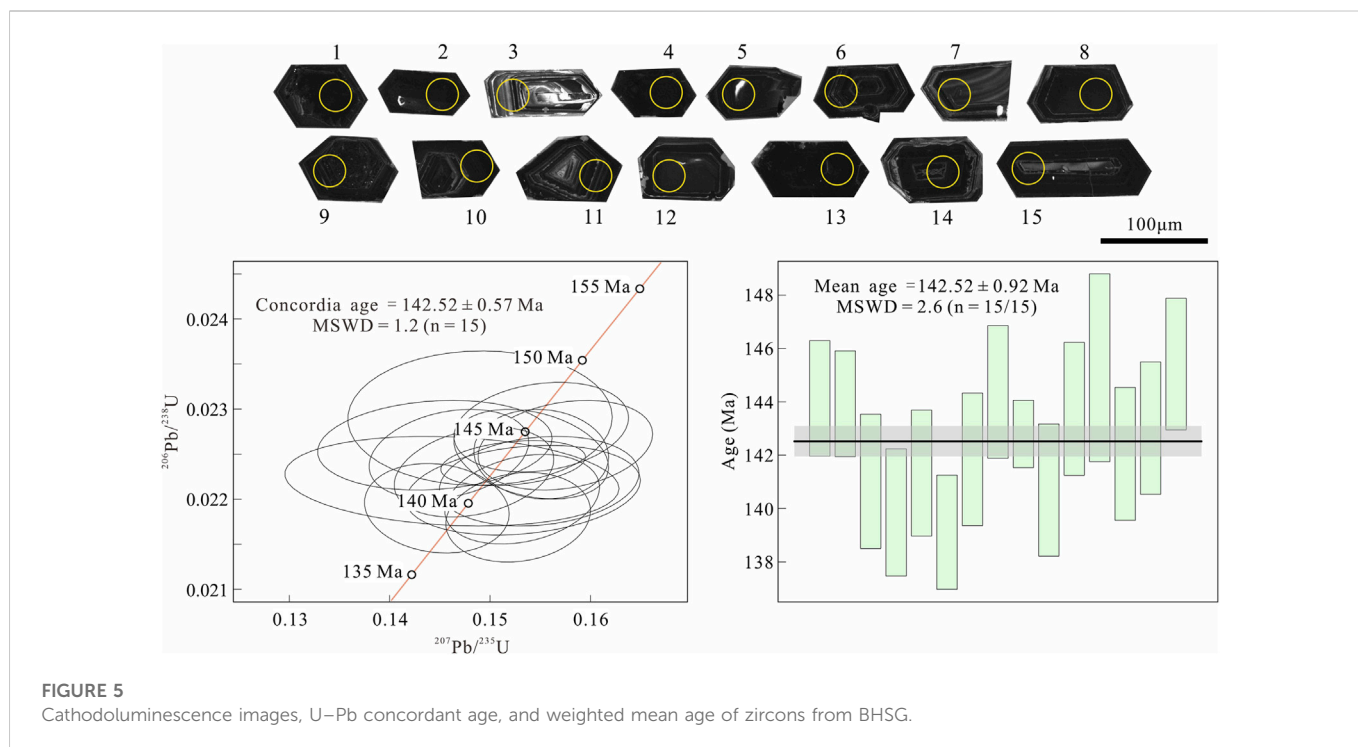


TABLE 2 LA-ICPMS U–Pb isotopic ratios and ages of the zircons from BHSg.

	$^{207}\text{Pb}/^{206}\text{Pb}$	1σ	$^{207}\text{Pb}/^{235}\text{U}$	1σ	$^{206}\text{Pb}/^{238}\text{U}$	1σ	$^{207}\text{Pb}/^{206}\text{Pb}$	1σ	$^{207}\text{Pb}/^{235}\text{U}$	1σ	$^{206}\text{Pb}/^{238}\text{U}$	1σ	Concordance (%)
1	0.0499	0.0010	0.1551	0.0027	0.0225	0.0002	190.82	46.29	146.40	2.35	143.22	0.99	97
2	0.0495	0.0012	0.1541	0.0031	0.0225	0.0002	168.60	55.55	145.49	2.76	143.25	1.25	98
3	0.0500	0.0015	0.1533	0.0047	0.0221	0.0002	194.53	70.36	144.86	4.17	140.67	1.29	97
4	0.0504	0.0010	0.1528	0.0029	0.0218	0.0002	216.74	46.29	144.39	2.51	139.20	1.10	96
5	0.0478	0.0023	0.1462	0.0067	0.0222	0.0002	100.09	111.10	138.59	5.94	141.25	1.04	98
6	0.0477	0.0011	0.1447	0.0029	0.0219	0.0002	83.43	83.32	137.22	2.60	139.85	1.02	98
7	0.0504	0.0013	0.1549	0.0040	0.0222	0.0002	213.04	89.80	146.23	3.50	141.75	1.39	96
8	0.0505	0.0011	0.1575	0.0035	0.0226	0.0002	220.44	82.40	148.54	3.08	143.80	1.47	96
9	0.0491	0.0009	0.1523	0.0029	0.0224	0.0001	153.79	44.44	143.93	2.52	142.92	0.92	99
10	0.0504	0.0010	0.1532	0.0031	0.0220	0.0002	213.04	48.14	144.76	2.74	140.19	0.97	96
11	0.0463	0.0015	0.1445	0.0047	0.0226	0.0002	13.06	87.03	137.02	4.17	144.34	1.17	94
12	0.0477	0.0018	0.1490	0.0053	0.0229	0.0003	83.43	88.88	141.03	4.72	146.05	1.66	96
13	0.0480	0.0010	0.1484	0.0032	0.0223	0.0002	98.24	47.22	140.46	2.85	142.29	1.05	98
14	0.0469	0.0010	0.1459	0.0032	0.0225	0.0002	42.69	51.85	138.31	2.80	143.51	1.26	96
15	0.0490	0.0011	0.1551	0.0035	0.0228	0.0002	146.38	51.85	146.40	3.05	145.46	1.06	99

4.3.1 Major- and trace-element composition

The BHSg samples have SiO₂ contents ranging from 76.03 to 77.41 wt%, Al₂O₃ contents ranging from 12.00 to 12.59 wt%, K₂O contents ranging from 3.70 to 4.27 wt%, Na₂O contents ranging from 1.05 to 3.04 wt%, CaO contents ranging from 0.80 to 1.88 wt%, TFe₂O₃

contents ranging from 1.05 to 1.35 wt%, MgO contents ranging from 0.12 to 0.35 wt%, and P₂O₅ contents ranging from 0.008 to 0.017 wt%. Overall, the petrochemical composition of BHSg shows obvious characteristics of high silicon and alkali contents, higher K₂O contents than Na₂O contents, and low CaO and P₂O₅ contents.

TABLE 3 Trace-element composition of the zircons from BHSG.

	La	Ce	Pr	Nd	Sm	Eu	Gd	Tb	Dy	Ho	Er	Tm	Yb	Lu	Hf	Th	U	Th/U
1	0.85	58	0.61	5.7	23.6	0.29	205	97	1,363	554	2,671	586	5,235	945	10,582	12,317	27,201	0.45
2	0.75	33	0.85	6.0	15.1	0.19	122	60	867	355	1,749	395	3,684	675	12,019	3,957	14,240	0.28
3	0.12	18	0.14	1.4	4.5	0.12	34	15	204	85	428	98	922	184	11,870	1,259	2,800	0.45
4	2.40	63	1.69	13.8	22.3	0.35	155	70	960	385	1,874	411	3,696	692	9,334	10,957	15,421	0.71
5	1.16	56	0.96	7.6	14.1	0.37	82	32	406	153	706	150	1,341	250	9,792	3,220	3,920	0.82
6	0.79	28	0.67	4.5	8.7	0.15	66	31	450	183	910	205	1,893	361	12,153	3,359	7,876	0.43
7	17.11	79	9.74	53.7	24.2	0.23	59	21	266	107	509	116	1,097	212	11,378	1,312	3,182	0.41
8	16.04	64	4.94	24.5	17.2	0.21	79	34	448	187	894	201	1,880	356	11,189	3,421	6,996	0.49
9	7.01	47	4.59	25.8	22.3	0.24	93	43	578	242	1,190	270	2,615	486	12,875	4,232	11,000	0.38
10	0.09	17	0.11	1.2	4.8	0.10	43	22	319	138	691	159	1,540	299	13,815	1,637	6,041	0.27
11	2.94	26	1.35	9.0	8.5	0.12	47	21	298	126	622	141	1,359	262	13,135	1,800	5,622	0.32
12	0.81	25	0.85	8.1	17.5	0.38	78	27	319	112	486	102	912	168	10,101	872	1,979	0.44
13	22.69	89	6.75	31.4	19.9	0.17	91	44	634	271	1,363	311	2,981	556	13,594	3,429	13,208	0.26
14	4.23	33	2.64	17.0	15.0	0.21	80	36	501	203	992	221	2,067	391	12,632	2,717	8,544	0.32
15	4.44	39	3.20	18.6	17.1	0.22	71	30	392	160	766	170	1,587	301	11,804	1,475	4,802	0.31

TABLE 4 Hf isotope ratios of the zircons from BHSG.

	Age (Ma)	$^{176}\text{Yb}/^{177}\text{Hf}$	$^{176}\text{Lu}/^{177}\text{Hf}$	$^{176}\text{Hf}/^{177}\text{Hf}$	$^{176}\text{Hf}/^{177}\text{Hf}_i$	$\epsilon_{\text{Hf}}(0)$	$\epsilon_{\text{Hf}}(t)$	TDM (Ma)	TDM2 (Ma)	$f_{\text{Lu/Hf}}$
1	144.8	0.088752181	0.003266624	0.282533434	0.2825246	-8.4	-5.6	1,081	1,551	-0.901608
2	143.2	0.14486411	0.005159885	0.282553131	0.2825393	-7.7	-5.1	1,111	1,518	-0.844582
3	140.7	0.078580832	0.002903214	0.282625302	0.2826177	-5.2	-2.4	934	1,345	-0.912554
4	143.5	0.136006445	0.00502482	0.282571554	0.2825581	-7.1	-4.4	1,078	1,476	-0.84865
5	141.3	0.10627651	0.003688358	0.282579275	0.2825695	-6.8	-4.1	1,025	1,452	-0.888905
6	139.9	0.121767181	0.004372213	0.282544319	0.2825329	-8.1	-5.4	1,099	1,535	-0.868307
7	141.8	0.061005395	0.002201254	0.282617852	0.282612	-5.5	-2.5	927	1,357	-0.933697
8	143.8	0.138355074	0.004937153	0.282593812	0.2825806	-6.3	-3.6	1,040	1,426	-0.851291
9	140.2	0.062311217	0.002277112	0.282606438	0.2826005	-5.9	-3.0	946	1,384	-0.931412
10	144.3	0.078730788	0.002849784	0.282606926	0.2825992	-5.8	-2.9	960	1,384	-0.914163
11	146.1	0.045653094	0.001655099	0.282592132	0.2825876	-6.4	-3.3	950	1,409	-0.950148
12	143.5	0.114812582	0.004071666	0.282574459	0.2825635	-7.0	-4.2	1,044	1,464	-0.877359
13	145.5	0.094450328	0.003419791	0.282570639	0.2825613	-7.1	-4.3	1,030	1,468	-0.896994

According to petrographic features (Figure 4), TAS diagram (Figure 6A), and Q'-ANOR normative diagram (Figure 6B), BHSG was classified by monzogranite. The aluminum saturation index (ASI) of BHSG ranges from 1.07 to 1.32, which showed weakly to strongly peraluminous features (Figure 6C). All the BHSG samples belonged to the high-K calc-alkaline series (Figure 6D).

The BHSG samples have total amounts of rare earth elements (REEs) ranging from 190.26×10^{-6} to 251.24×10^{-6} , with an average of 217.54×10^{-6} . The difference between light and heavy REEs is not obvious, and the light REEs are slightly enriched with $(\text{La}/\text{Yb})_N$

values ranging from 1.41 to 2.53. The depletion of Eu is obvious, showing relatively flat REE patterns (Figure 7A). In the primitive mantle-normalized diagram of trace elements (Figure 7B), it is shown that some elements such as Cs, Rb, Th, U, and Pb are obviously enriched, and some elements such as Ba, Sr, P, and Ti are obviously negative.

4.3.2 Alteration effect

Alteration can be observed both on hand specimens and under a microscope, which is mainly manifested by sericitization and

TABLE 5 Whole-rock major-element composition of BHSg and standard samples.

Sample	BHSg1	BHSg2	BHSg3	BHSg4	BHSg5	Standard sample	Standard value	Standard sample	Standard value	Standard sample	Standard value
SiO ₂	76.03	77.41	76.26	76.40	76.19	72.82	72.83	44.71	44.64	59.60	59.68
TiO ₂	0.06	0.08	0.08	0.09	0.09	0.29	0.29	2.39	2.37	0.75	0.77
Al ₂ O ₃	12.29	12.00	12.59	12.12	12.16	13.38	13.40	13.77	13.83	16.64	16.56
TFe ₂ O ₃	1.25	1.27	1.34	1.35	1.05	2.12	2.14	13.54	13.40	6.04	6.06
MnO	0.06	0.03	0.03	0.03	0.03	0.06	0.06	0.17	0.17	0.09	0.09
MgO	0.35	0.20	0.20	0.15	0.12	0.41	0.42	7.73	7.77	2.75	2.81
CaO	1.88	1.04	0.80	0.86	1.25	1.54	1.55	8.87	8.81	4.70	4.72
Na ₂ O	1.05	2.49	2.66	2.73	3.04	3.08	3.13	3.33	3.38	4.02	4.05
K ₂ O	3.82	3.70	4.09	4.27	3.76	4.98	5.01	2.28	2.32	3.48	3.50
P ₂ O ₅	0.008	0.015	0.014	0.017	0.014	0.09	0.09	0.94	0.95	0.33	0.34
LOI	2.84	1.60	1.37	1.37	1.61	0.75	0.69	2.03	2.24	1.04	1.04
SUM	99.63	99.84	99.43	99.39	99.30	99.52	99.61	99.75	99.88	99.43	99.63
FeO	0.81	0.87	0.92	0.93	0.69	1.02	1.02	7.53	7.60	3.04	3.08
TFeO	1.13	1.15	1.20	1.22	0.94						
Q	51.96	46.59	43.44	42.44	41.87						
An	3.13	2.09	2.41	1.52	0.87						
Ab	23.34	22.26	24.69	25.75	22.75						
Or	9.19	21.44	22.96	23.59	26.38						
C	9.58	5.17	3.97	4.26	6.25						
Hy	0.89	0.51	0.51	0.39	0.31						
Il	1.24	1.30	1.37	1.38	0.97						
Mt	0.53	0.45	0.47	0.47	0.42						
Ap	0.12	0.15	0.16	0.17	0.17						
Zr	0.02	0.04	0.03	0.04	0.03						
DI	84.36	90.15	90.94	91.64	90.85						
A/NK	2.10	1.48	1.43	1.33	1.34						
A/CNK (ASI)	1.32	1.20	1.23	1.14	1.07						
Na ₂ O+K ₂ O	4.87	6.18	6.75	7.00	6.80						

(Continued on following page)

TABLE 5 (Continued) Whole-rock major-element composition of BHSBG and standard samples.

Sample	BHSG1	BHSG2	BHSG3	BHSG4	BHSG5	Standard sample	Standard value	Standard sample	Standard value
K ₂ O/Na ₂ O	3.64	1.49	1.54	1.56	1.24				
FeOT/MgO	3.27	5.67	6.05	8.01	7.84				
T _{Zr}	796.62	794.53	805.26	796.96	787.97				

argillation of feldspar phenocrysts (Figures 4D–G). The alteration effect should be evaluated before the geochemistry analysis. Large ion lithophile elements (LILEs) and some major elements, such as calcium (Ca), sodium (Na), potassium (K), rubidium (Rb), barium (Ba), and strontium (Sr), are generally mobile, whereas high field strength elements (HFSEs), rare earth elements (REEs), and some major elements, such as titanium (Ti), aluminum (Al), phosphorus (P), iron (Fe), niobium (Nb), tantalum (Ta), zirconium (Zr), and hafnium (Hf), are relatively immobile during hydrothermal alteration (Smith and Smith, 1976; Maclean, 1990).

The loss on ignition (LOI) is useful as an actual estimate of total volatiles in certain geologic studies and as an indication of volcanic rock alteration resulting from hydration or calcitization of mafic minerals (Lechler and Desilets, 1987). In the diagrams of correlation between mobile elements and LOI (Figure 8), the contents of SiO₂, TiO₂, Al₂O₃, TFeO, K₂O, P₂O₅, Rb, Ba, and Sr exhibit weak or no variation with increasing LOI, suggesting a weak or no alteration effect on these elements. As to the REEs and the other trace elements, although the LOI values of the five samples of BHSBG are variable, the chondrite-normalized REE patterns and primitive mantle-normalized multi-element patterns are highly consistent (Figure 7), suggesting a weak or no alteration effect on these elements. Otherwise, the contents of CaO, Na₂O, and MgO changed with increasing LOI (Figures 8E–G), suggesting the sample BHSBG1 may be affected. The abnormal Na₂O content may be responsible for the discrete distribution of the sample BHSBG1 in the Q'–ANOR normative diagram and A/NK–A/CNK diagram (Figure 6C).

The alteration box plot, combining the Ishikawa alteration index (AI) and the chlorite–carbonate–pyrite index (CCPI), is a powerful means of understanding the relationship between mineralogy, petrogeochemistry, and intensity of alteration (Large et al., 2001). The CCPI vs. AI plot was divided into two parts by the black dotted line in the middle (Figure 9). Hydrothermal alteration produced trends to the upper right, and diagenetic alteration produced trends to the lower left. Meanwhile, a least altered box was defined by AI values ranging from 20 to 65 and CCPI values ranging from 15 to 85 (Large et al., 2001). The contents of major elements of BHSBG presented AI values ranging from 47.47 to 58.72 and CCPI values ranging from 13.5 to 23.23, which are mainly plotted within the least altered box and related to the diagenetic trends in the lower left part (Figure 9). According to this plot, slight diagenetic alteration and no hydrothermal alteration may have occurred, which may be related to the replacement of albite by K-feldspar and sericite.

Therefore, the alteration effect on all trace elements, including REEs, is negligible. The CaO, Na₂O, and MgO contents of sample BHSBG1 have been affected by diagenetic alteration, whereas the alteration effect on major-element contents of the other samples should be finite.

5 Discussion

5.1 Magmatic differentiation

The BHSBG has high SiO₂ content and high differentiation index (Di), indicating a high degree of differentiation. The whole-rock Zr/Hf and Nb/Ta ratios are reliable indicators of the degree of granitic magma differentiation because Zr and Hf, as well as Nb and Ta, are

TABLE 6 Whole-rock trace-element composition of BHSg and standard samples.

Sample	BHSg1	BHSg2	BHSg3	BHSg4	BHSg5	AGV-2	Standard value	BCR-2	Standard value	RGM-2	Standard value
Ba	234.77	257.39	307.41	147.06	353.71	1,122	1,130	668	677	834	810
Rb	248.17	215.90	240.37	223.62	230.68	67.3	66.3	46.2	46.9	150	150
Sr	94.39	74.76	78.91	79.05	103.08	669	661	339	340	111	108
Zr	128.69	137.99	155.09	152.16	146.16	232	230	182	184	229	220
Nb	41.79	36.82	40.76	38.83	38.46	14.4	14.5	12.4	12.6	9.36	9.30
Ni	0.38	0.35	0.37	0.31	0.40	19.1	20.0	12.6	13.0	2.18	5.20
Co	0.44	0.99	1.21	0.86	2.61	16.2	16.0	37.7	37.0	2.07	2.0
Zn	46.98	130.05	185.44	118.26	78.45	87.9	86.0	131	133	31.5	32.0
Cr	0.46	0.54	0.57	0.53	0.56	16.1	16.2	15.3	16.5	3.19	5.90
La	24.55	32.22	30.92	40.24	33.15	38.4	37.9	25.0	24.9	23.2	24.0
Ce	60.90	77.25	70.89	89.68	76.97	70.2	68.6	52.4	52.9	46.5	47.0
Pr	7.45	9.01	8.52	10.84	9.44	8.11	7.84	6.61	6.70	5.29	5.36
Nd	28.54	34.36	33.83	41.11	35.54	30.7	30.5	28.9	28.7	19.5	19.0
Sm	9.08	9.34	9.50	10.98	9.86	5.64	5.49	6.63	6.58	4.00	4.30
Eu	0.20	0.23	0.24	0.28	0.24	1.55	1.54	2.00	1.96	0.61	0.66
Gd	10.67	10.39	10.65	11.85	10.95	4.67	4.52	6.81	6.75	3.64	3.70
Tb	2.34	2.04	2.13	2.33	2.13	0.63	0.64	1.08	1.07	0.62	0.66
Dy	15.25	13.44	14.42	15.09	14.33	3.59	3.47	6.58	6.41	3.85	4.10
Ho	3.40	3.05	3.27	3.32	3.14	0.69	0.65	1.30	1.28	0.78	0.82
Er	11.71	9.86	10.96	10.67	10.33	1.85	1.81	3.71	3.66	2.27	2.35
Tm	1.80	1.55	1.71	1.68	1.66	0.26	0.26	0.53	0.54	0.37	0.37
Yb	12.48	10.50	11.64	11.41	11.41	1.68	1.62	3.44	3.38	2.53	2.60
Lu	1.89	1.61	1.82	1.76	1.71	0.26	0.25	0.52	0.50	0.38	0.40
Y	106.32	92.63	100.88	101.84	100.45	20.4	20.0	36.0	37.0	23.9	23.2
Cs	35.80	11.89	11.08	7.95	11.12	1.10	1.16	1.04	1.10	9.73	9.60
Ta	6.17	5.05	5.61	5.30	5.26	0.88	0.87	0.78	0.78	0.92	0.95
Hf	6.06	5.99	6.80	6.88	6.35	5.27	5.0	4.96	4.90	5.90	6.20
Ga	19.21	19.34	21.52	21.99	18.48	20.9	20.0	22.7	23.0	16.5	16.5
Cu	72.41	101.28	178.43	105.41	309.28	53.0	53.0	20.8	19.7	10.2	9.60
Pb	50.55	143.60	142.51	193.20	74.41	13.4	13.2	10.2	11.0	19.6	19.3
Sn	9.10	6.26	6.10	8.94	7.19	1.99	1.83	2.03	2.03	3.25	3.34
Th	52.67	53.07	55.08	55.69	56.53	6.32	6.10	5.96	5.70	14.7	15.1
U	19.55	17.30	19.30	18.22	19.28	1.93	1.86	1.73	1.69	5.68	5.80
Li	26.99	24.18	22.70	22.14	22.58	10.2	11.0	8.71	9.0	59.1	57.0
Be	15.99	14.35	15.34	12.52	13.52	2.22	2.30	1.96		2.50	2.37
Sc	0.17	0.91	0.91	1.43	0.85	12.5	13.0	33.7	33.0	4.21	4.40
V	3.85	3.04	3.24	2.94	3.47	121	120	416	416	14.1	13.0
Zr/Hf	21.25	23.03	22.81	22.13	23.02						

(Continued on following page)

TABLE 6 (Continued) Whole-rock trace-element composition of BHSg and standard samples.

Sample	BHSG1	BHSG2	BHSG3	BHSG4	BHSG5	AGV-2	Standard value	BCR-2	Standard value	RGM-2	Standard value
Nb/Ta	6.78	7.30	7.26	7.33	7.31						
Zr + Nb + Ce + Y	337.70	344.69	367.62	382.51	362.04						
10,000 Ga/Al	2.95	3.04	3.23	3.43	2.87						
ΣREE	190.26	214.83	210.52	251.24	220.85						
ΣLREE	130.73	162.40	153.91	193.13	165.20						
ΣHREE	59.53	52.43	56.61	58.11	55.65						
(La/Yb) _N	1.41	2.20	1.90	2.53	2.08						
Eu/Eu*	0.062	0.070	0.074	0.074	0.071						

Eu/Eu* = Eu/SQRT (Sm×Gd); The element values, namely Eu, Sm and Gd, in this formula are chondrite-normalized values.

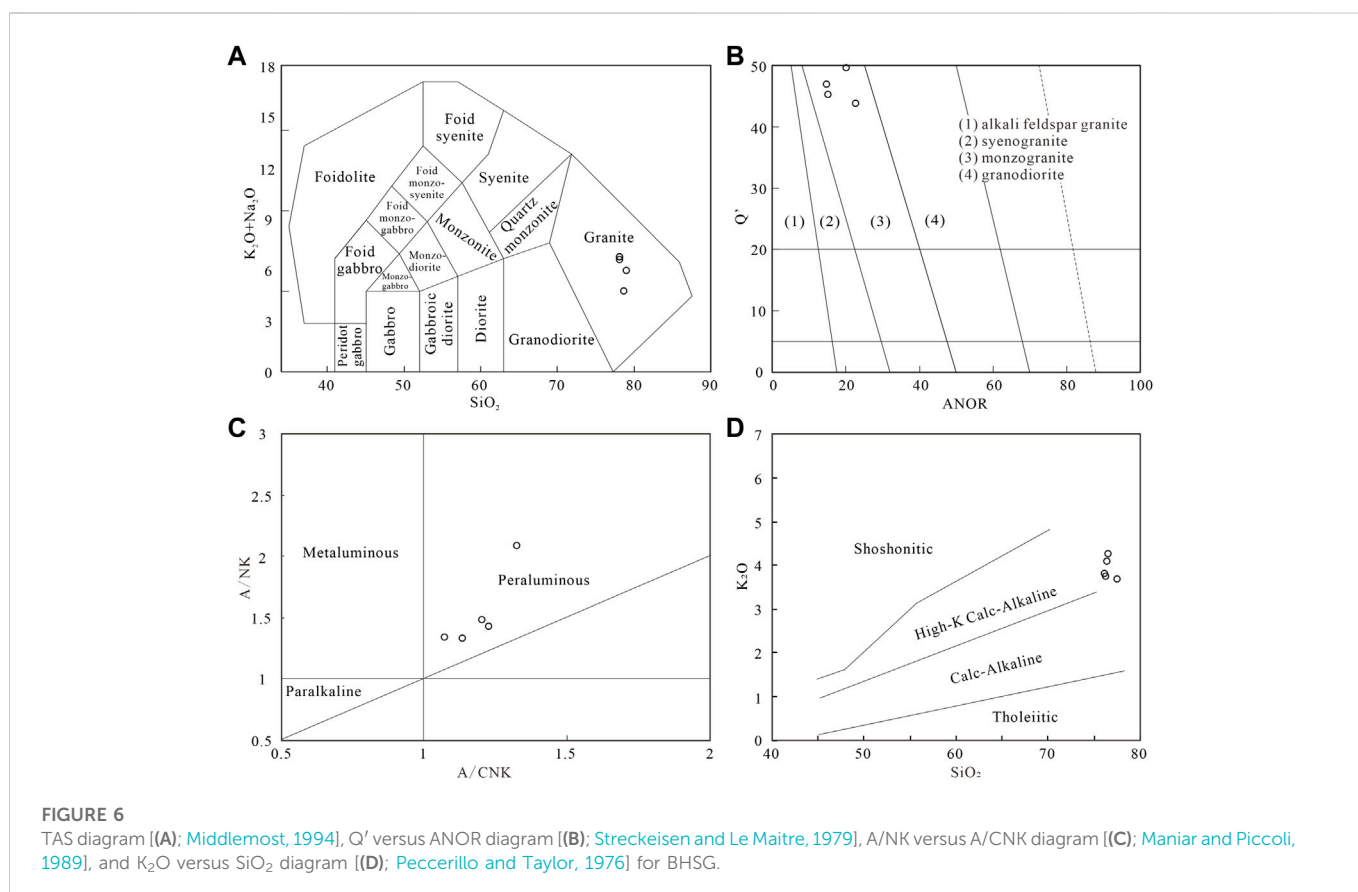


FIGURE 6

TAS diagram [(A); Middlemost, 1994], Q' versus ANOR diagram [(B); Streckeisen and Le Maitre, 1979], A/NK versus A/CNK diagram [(C); Maniar and Piccoli, 1989], and K₂O versus SiO₂ diagram [(D); Peccerillo and Taylor, 1976] for BHSg.

elements considered to be “geochemical twins” having the same charge and a similar ionic radius (Ballouard et al., 2016). Also, they have similar geochemical properties and should not be fractionated during most geological processes (Goldschmidt, 1937). However, Zr/Hf and Nb/Ta ratios will decrease during fractional crystallization in granites and the interaction with late magmatic fluids in evolved peraluminous granites (Ballouard et al., 2015; Dostal et al., 2015; Wu et al., 2017). The whole-rock Zr/Hf and Nb/Ta ratios of BHSg range from 21.25 to 23.03 and from 6.78 to 7.33. The Zr/Hf ratios are lower than the maximum of the magmatic–hydrothermal transition system (Zr/Hf <

26; Bau, 1996), and Nb/Ta ratios were close to the fingerprint of the magmatic–hydrothermal transition system (Nb/Ta < 5, Ballouard et al., 2016; Figure 10). Moreover, BHSg has other typical characteristics of highly fractionated granites, such as low content of REEs, low ratio between light and heavy REEs, and significant negative Eu anomaly (Figure 7A; Gelman et al., 2014; Miller and Mittlefehldt, 1982; Miller and Mittlefehldt, 1984).

The low total REE contents and the small ratios between light and heavy REEs of BHSg indicate fractional crystallization of REE-rich minerals such as zircon, monazite, epidote, and xenotime. The

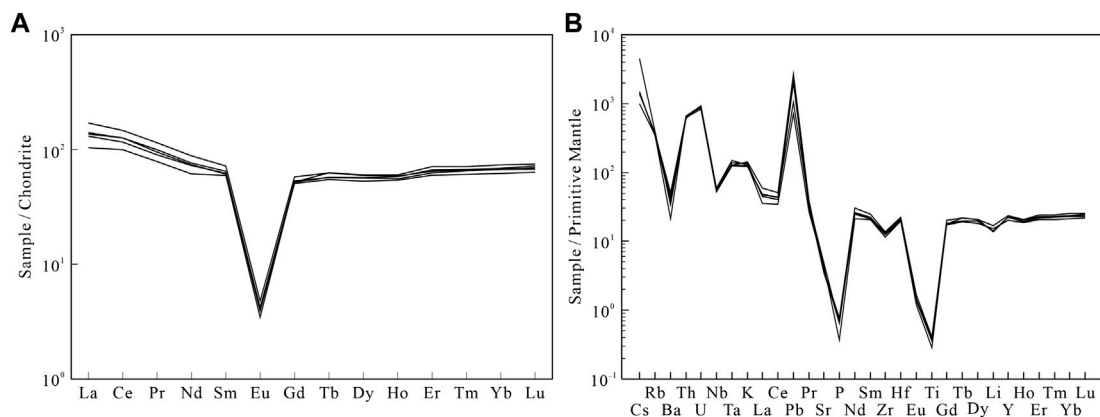


FIGURE 7

Chondrite-normalized REE patterns (A) and primitive mantle-normalized multi-element diagrams (B) for BHS and FQSG (the normalization values after Sun and McDonough, 1989).

apparent depletion of Eu, Ba, and Sr reflects the significant fractional crystallization of plagioclase and/or K-feldspar. The apparent depletion of P reflects the significant fractional crystallization of apatite.

5.2 Geochemical affinity to highly evolved aluminous A-type granite

The peraluminous characteristics of BHS reflect geochemical affinity to S-type, highly evolved I-type, and A-type granitoids (Chappell and White, 1992; Eby, 1992). S-type and I-type granitoids can be distinguished by P_2O_5 content and their relation to SiO_2 . The P_2O_5 content increases with crystallization differentiation in S-type granite and decreases with crystallization differentiation in weakly peraluminous I-type granite (Chappell and White, 1992). P_2O_5 abundance is also a reliable criterion for distinguishing A-type and S-type granites (Bonin, 2007). BHS has an extremely low P_2O_5 content ranging from 0.008 wt.% to 0.017 wt.%, showing affinity to highly evolved peraluminous A-type granite and rejecting the possibility of S-type granite (Supplementary Figure S1) because highly evolved S-type granites have high P_2O_5 contents ranging from 0.4 to 1.6 wt.% (Bonin, 2007).

I- and S-type granites are distinguished by source rocks, while the identification of A-type granite emphasizes its chemical composition. A-type granite was characterized by high SiO_2 ; high FeO_7/MgO ; high total alkali content; high K_2O/Na_2O ; high REE (except Eu), Zr, Nb, and Ta abundances; and low CaO, Ba, Sr, and Eu abundances (Collins et al., 1982; Eby, 1992; Eby and Kochhar, 1990; Loiseau and Wones, 1979; Whalen et al., 1987). In terms of major elements, the diagrams related to K_2O , Na_2O , and CaO could not distinguish A-type granite from other granites (Supplementary Figure S2) because the total alkali ($K_2O + Na_2O$) content and CaO content of different granites in origin are similar when the SiO_2 content is greater than 74 wt.% (Eby and Kochhar, 1990). In terms of trace elements, the discriminant diagrams based on Ga–Zr–Nb–Ce–Y gave a clear distinction of BHS as A-type

granite (Figure 11). Although the data are plotted near the boundary between A-type and the other type granites in Zr-related diagrams (Figure 11), they do not affect the discrimination of A-type granite for BHS. This can be attributed to the high differentiation of BHS, which resulted in the crystallization separation of zircons and then the decrease of Zr content in the melt (King et al., 2001). Moreover, the BHS samples all fell in the WPG (“Within Plate Granite”; Supplementary Figure S3; Pearce et al., 1984) zone, which supported the validity of the diagrams based on Ga–Zr–Nb–Ce–Y (Eby and Kochhar, 1990).

The most essential characteristic of A-type granite is its high temperature. The average crystallization temperature of aluminous A-type granites obtained by a zircon saturation thermometer is usually over 800°C (King et al., 1997). The zirconium saturation thermometer presented a mean temperature of 796°C for BHS (Watson and Harrison, 1983). High Zr content is the chief criterion for identifying A-type granite, but most felsic A-type granites have lower Zr contents due to removal of zircon during fractionation, which makes the Zr content and further the calculated zircon saturation temperature both lower (King et al., 2001; King et al., 1997). Petrographic observation shows zircon wrapped in biotite phenocryst (Figure 4H), indicating that zircon is a fractionated mineral and zirconium has reached saturation in the early stage of fractional crystallization. BHS is a highly differentiated granite which has undergone strong fractional crystallization, indicating that zirconium has been further lost after reaching saturation in magma. It means that the actual magma temperature is significantly higher than the calculated zirconium saturation temperature and should be higher than 800°C.

Furthermore, the A-type granitoids can be chemically subdivided into two groups, namely, A_1 -subtype granite, which has similar element ratios to oceanic island basalts, and A_2 -subtype granite, which has similar element ratios to average crust and island arc basalts (Eby, 1992). BHS was subdivided into A_2 -subtype granite according to the triangle diagram of incompatible elements (Figure 12). Therefore, BHS is a highly evolved aluminous A-type granite.

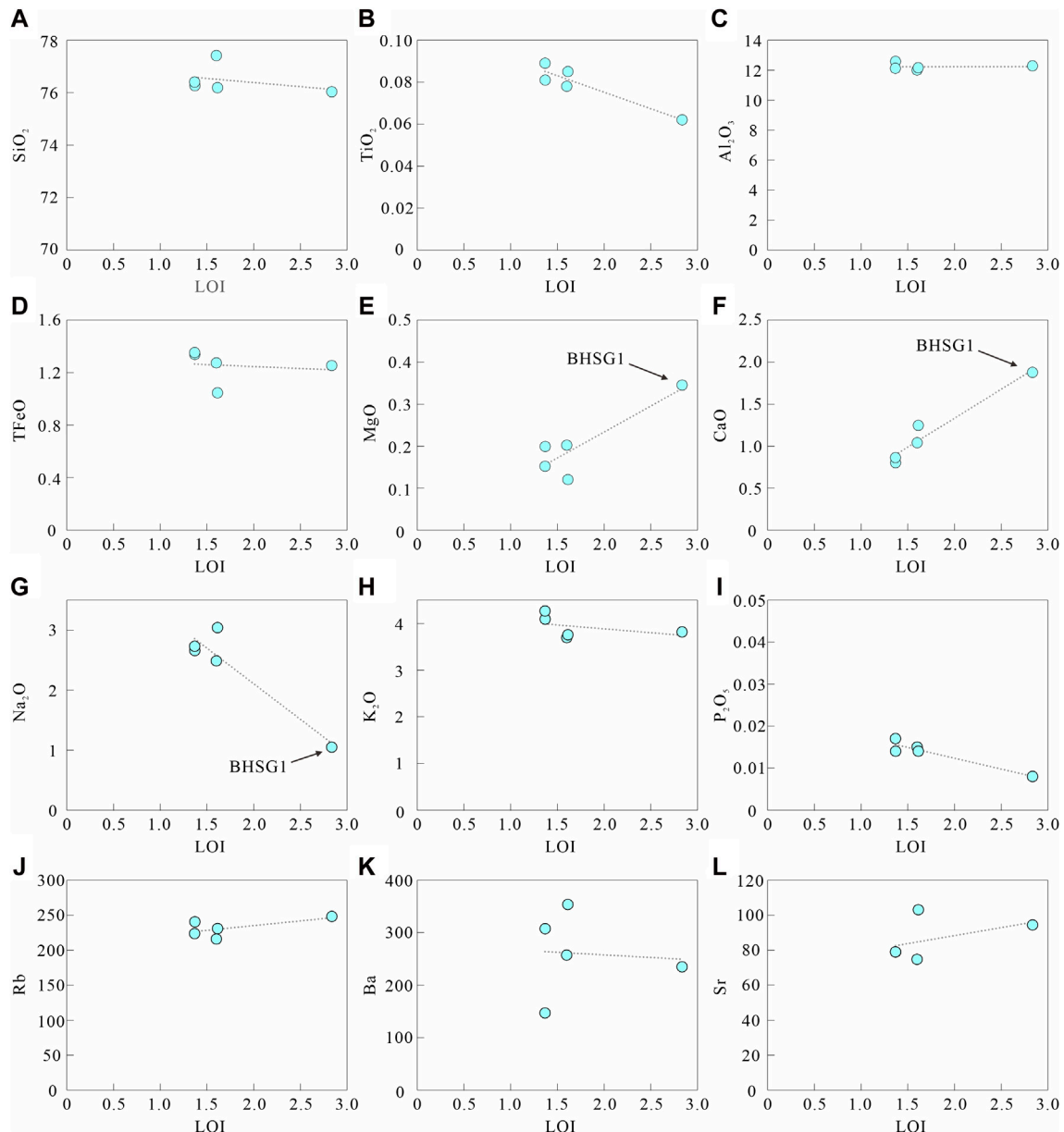


FIGURE 8
LOI versus major elements, Rb, Ba, and Sr plots. The label BHS G1 refers to sample BHS G1 in [Table 5](#).

5.3 Magmatic origin

The $\epsilon_{\text{Hf}}(t)$ values of BHS G and Neoproterozoic arc-related magmatic rocks in the Shuangqiaoshan Group mainly fall near the same crustal evolution line ([Figure 13](#)), indicating the similarity of their source. The quartz–keratophyre and tuff are from the base of the Shuangqiaoshan Group and formed in a syn-orogenic back-arc foreland setting at *ca.* 880 Ma. The $\epsilon_{\text{Hf}}(t)$ values of quartz–keratophyre and tuff intersect the depleted mantle curve, reflecting the material contribution of the depleted mantle endmember and Neoproterozoic crustal–mantle interactions during the Neoproterozoic orogeny to these volcanic rocks. The *ca.* 800 Ma

gabbro from the Shuangqiaoshan Group had arc-like geochemical features, which was considered to generate from the partial melting of juvenile crustal materials resulting from Neoproterozoic subduction ([Wang et al., 2008](#)). The model age of BHS G is basically the same as that of *ca.* 800 Ma gabbro, and there is a large overlap with *ca.* 880 Ma volcanic rocks, suggesting the source of BHS G is similar to that of the *ca.* 800 Ma gabbro and is also related to the juvenile crust formed during Neoproterozoic arc-related magmatism.

The source discriminant diagram indicates that tonalites and metasediments are potential sources of BHS G ([Figure 14](#)). Tonalite is a representative component of TTG rock assemblage, which is the main product of crustal growth in the subduction and/or

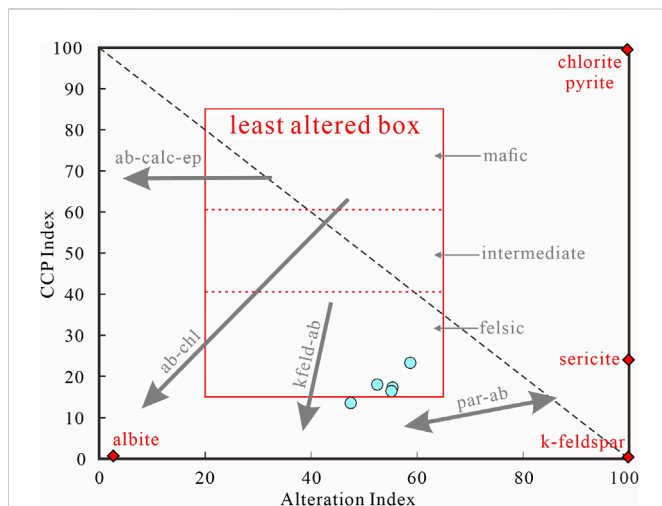


FIGURE 9

Alteration box plot with fields of diagenetic alteration (Large et al., 2001). The arrows show the common trends for diagenetic alteration. Abbreviations: ab-calc-ep, epidote–calcite ± albite trend; ab-chl, albite–chlorite trend; k-feld-ab, early diagenetic trend of K-feldspar replacing albite; par-ab, sericite–albite trend.

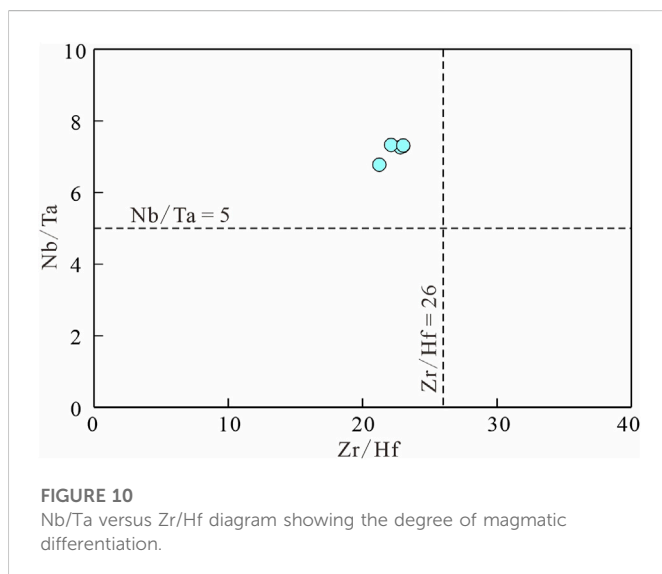


FIGURE 10

Nb/Ta versus Zr/Hf diagram showing the degree of magmatic differentiation.

collision zones (Laurent et al., 2020), and metasediments could originate from the weathering products of TTG. So, the source rocks distinguished are consistent with the preceding interpretation of Hf isotopes and the origin of A₂-type granite, whose source was originally formed by subduction or continent–continent collision (Eby, 1992).

BHSG has high heavy REE content and obvious Eu negative anomaly (Figure 7A), indicating that the magma was derived from an intracrustal source at a relatively shallow depth where plagioclase is stable and garnet is unstable. Therefore, BHSG is thought to have

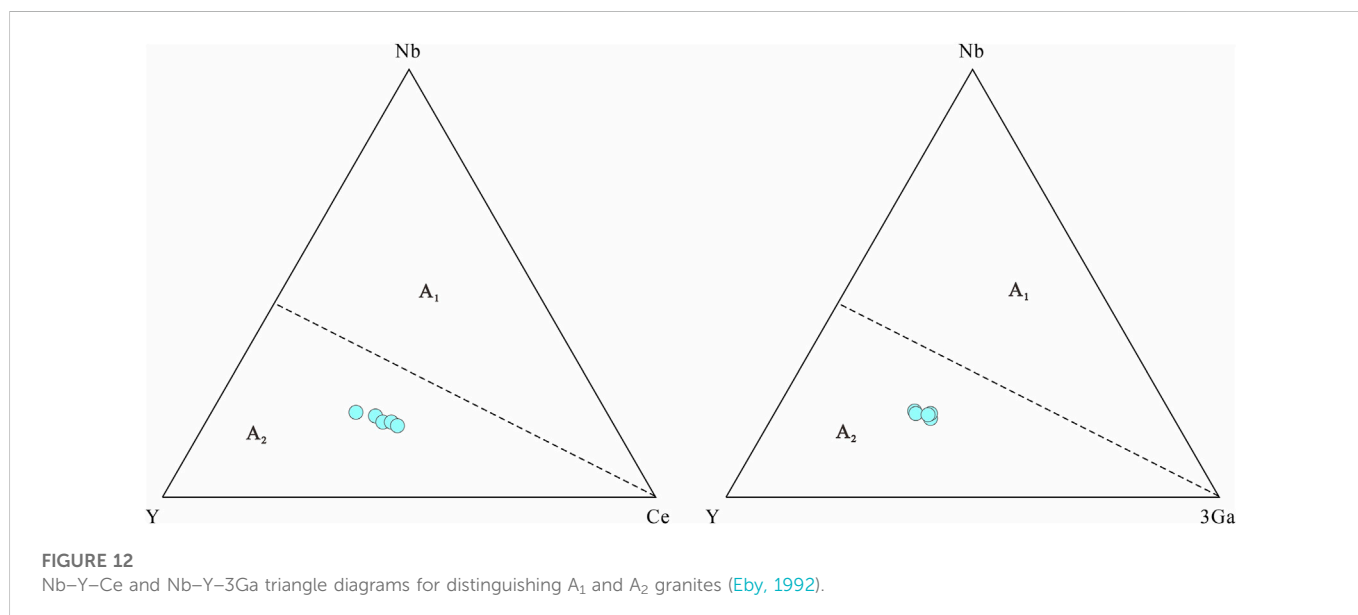
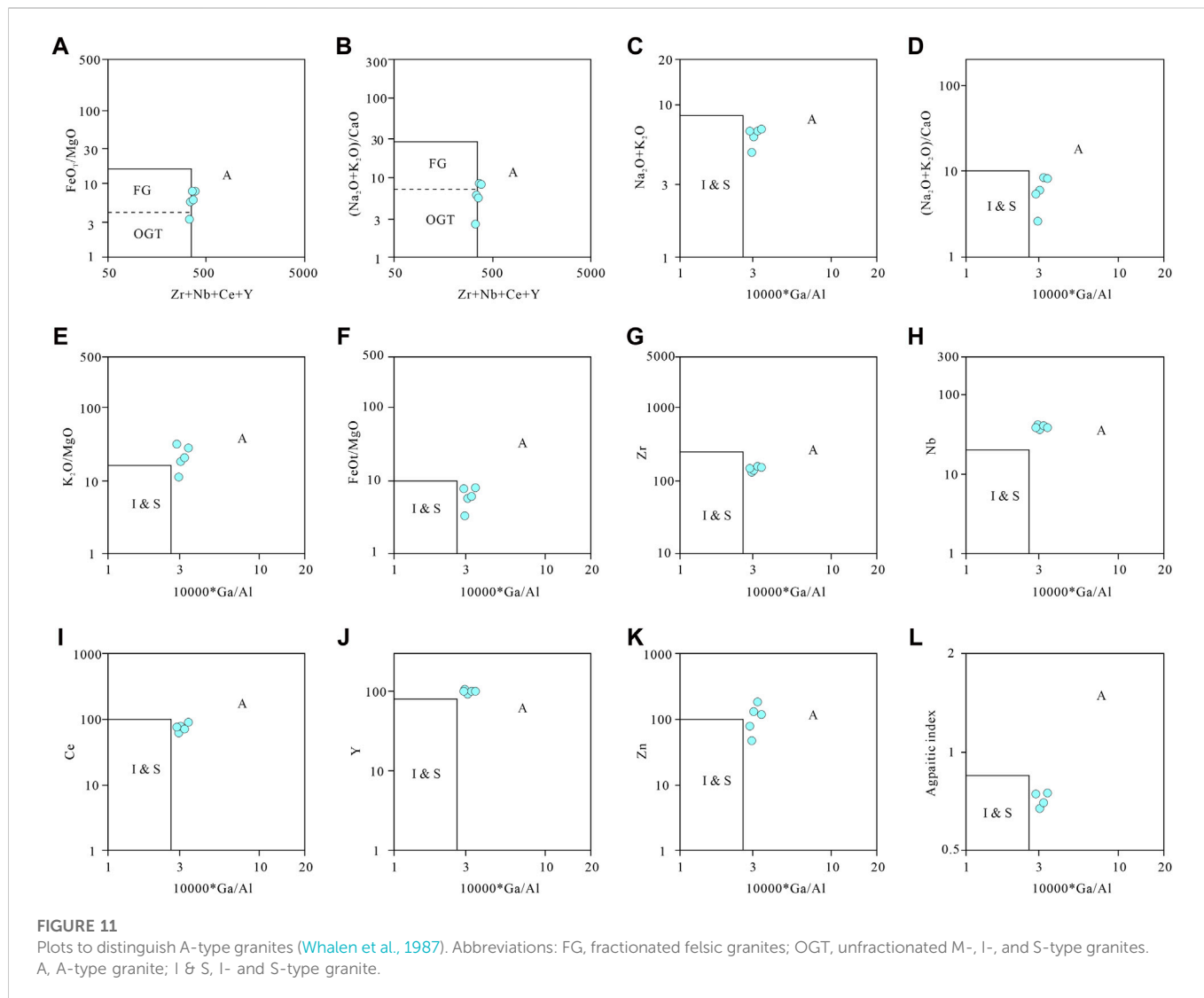
originated mainly from partial melting of a reworked juvenile crust composed of TTGs and its weathered sediments related to Neoproterozoic arc-related magmatism.

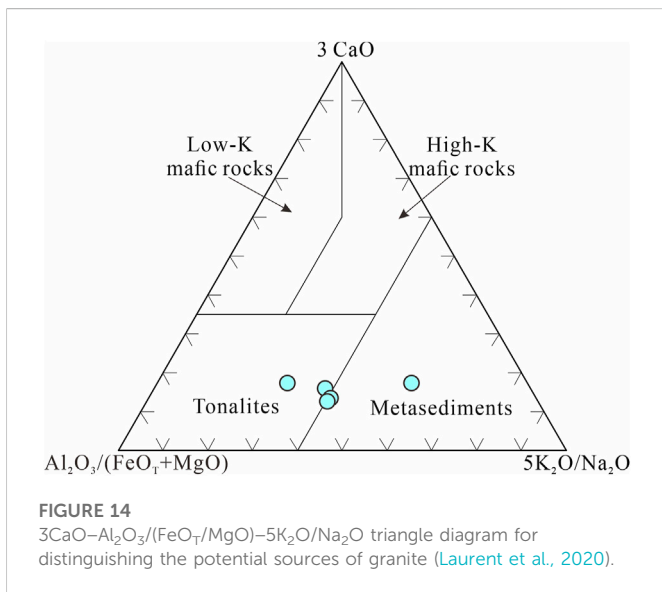
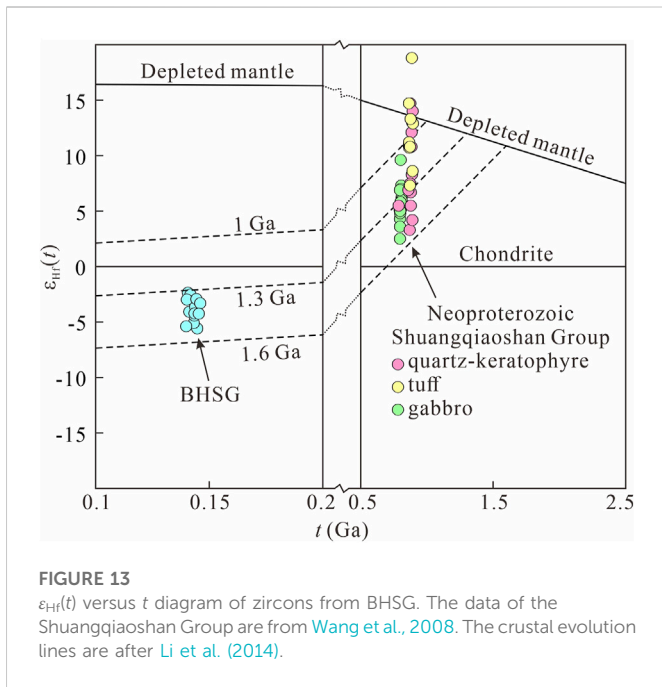
5.4 Onset of Early Cretaceous extension in the EJM and structural reactivation of the NEJFZ

Systematic geological records related to the Cretaceous extension in the SCB are concentrated in CT, SR, and JM (Figure 1; Li et al., 2022). The extension in these distribution ranges was expressed by varying combinations and intensities of those geological records. The CT includes the coastal area east of the ZDFZ, where the Cretaceous extension is mainly characterized by the concentrated distribution of volcanic rocks and intrusive rocks and accompanied by extensional basins. Also, the CT is the most important distribution area of Cretaceous magmatism (Zhou and Li, 2000). The Cretaceous extension in SR is mainly characterized by a continuous series of elongated basins, normal faults, volcanic rocks, intrusive rocks, and extensional domes. These normal faults act as basin-bounding structures controlling Cretaceous basins' opening and sedimentary infilling (Li et al., 2022). The Cretaceous extension in the JM is distinctive and characterized by several extensional domes, including Yuechengling (Chu et al., 2019), Hengshan (Li et al., 2013), Wugongshan (Faure et al., 1996; Lou et al., 2005), Dayunshan (Ji et al., 2018a; Ji et al., 2018b), and Lushan (Lin et al., 2000; Wang et al., 2013). Also, extensional basins and intrusive rocks also developed in the JM.

In the CT and SR, the earliest extensional basins can be constrained by the age of volcanic rocks since volcanic rocks are mostly present in the lower part of the sedimentary sequence of the basins. The onset of the Cretaceous extension in the CT and SR can, therefore, be constrained to 145–140 Ma (Figure 15). There may be no significant difference in the onset of the extension in different parts of the CT according to the age of volcanic rocks from the southeastern Zhejiang Province and eastern Fujian and Guangdong provinces (Guo et al., 2012; Li et al., 2014; Liu et al., 2012), whereas the onset of the extension in the northeast part of the SR may be earlier than that in the inland according to the age of volcanic rocks from the northwestern Zhejiang Province and Xiangshan Basin (Figure 15; Liu et al., 2014; Yang et al., 2011).

In the JM, the onset of the Cretaceous extension was mainly constrained by the detachment fault with low-temperature thermochronology. In the WJM, the detachment fault in the YCL extensional dome began to move at ca. 140 Ma (Chu et al., 2019). In the EJM, the detachment faults in Hengshan, Dayunshan, and Lushan extensional domes began to move at ca. 136 Ma (Li et al., 2013), ca. 132 (Ji et al., 2018a), and ca. 140 Ma (Zhu et al., 2010), respectively. Rare A-type granite formed at ca. 134 Ma (Yang et al., 2021). Combined with the newly reported chronological data of BHSG A-type granite, we argue that the Cretaceous lithospheric extension in the EJM has started as early as ca. 145–140 Ma, indicating that a lithosphere extensional regime has probably dominated the CT, SR, and JM during 145–140 Ma.





The following points are noted: first, the onset of the CT, SR, and JM was almost at the same time, which reflected that these geological units were in a unified tectonic stress field and the source of tectonic stress was controlled by a unified dynamic mechanism. The attenuation of extension-related geological records, especially magmatism, from the coast to the inland indicates that the source

of tectonic stress is from the coast, namely, the subduction between eastern Eurasia and the oceanic plate in its east. Second, it does not mean that the entire EJM or JM has been dominated by the lithosphere extensional regime. The spatial distribution of all the extension-related geological records in the SR, the extensional domes in the JM, and BHSG A-type granite consistently exhibit their close correlations with inherited structures. The control of inherited structures over lithosphere extension has been demonstrated in a specific structural deformation study in the JM (Li et al., 2013) and adopted to interpret the petrogenesis and evolution of tectonics in South China (Chu et al., 2019; Pan et al., 2018; Sun et al., 2018; Suo et al., 2019; Wang et al., 2015; Yu et al., 2006; Zhang et al., 2022). Although the tectonic stress field is consistent, the distribution of strain and magmatism is obviously inhomogenous, which shows the dominant control of the inherited structure on the tectono-thermal events in the intraplate area.

A-type granites were thought to form in anorogenic setting at the earliest (Loiselle and Wones, 1979) and were later found to form in a large range of geodynamic contexts (Bonin, 2007), including post-collisional and post-orogenic settings (Sylvester, 1989; Rogers and Greenberg, 1990). According to the original research of Eby (1992), the tectonic setting of A₁-subtype granites was related to hotspots, plumes, or continental rift zones located in anorogenic settings, while the tectonic setting of A₂-subtype granites was related to post-collisional and anorogenic settings.

In the Early Mesozoic, South China was in an intracontinental tectonic setting, and significant intracontinental orogeny took place, including multi-stage compressive tectonic deformation during Indosinian and Yanshanian periods (Li et al., 2016; Chu et al., 2015). Furthermore, a transition from the Tethyan tectonic domain to the Paleo-Pacific tectonic domain in South China has been proven by structural deformation, sedimentary basin, and magmatism studies (Gan et al., 2021; Xu et al., 2019; Zhang et al., 2009). The transition likely occurred during the Early-Middle Jurassic and completed at 165 ± 5 Ma (Gan et al., 2021; Xu et al., 2019). Therefore, the South China Block was dominated by the Paleo-Pacific tectonic domain during the Late Jurassic–Early Cretaceous. Extensive Jurassic–Cretaceous magmatism in southeast China occurred due to subduction of the Paleo-Pacific plate (Li and Li, 2007; Suo et al., 2019; Zhou and Li, 2000; Zhou et al., 2006). Moreover, the oceanward-younging Jurassic–Cretaceous granites and volcanic rocks have been recognized (Zhou and Li, 2000) and were explained by oceanic slab rollback and arc retreat (Li and Li, 2007; Li et al., 2021; Liu et al., 2018). The slab rollback and arc retreat may have provided an extensional tectonic setting for the eastern Jiangnan Massif which was intracontinental and away from the subduction zone. Therefore, we argue that the origin of BHSG is controlled by the reactivation of the NEJFZ triggered by the Early Cretaceous subduction process along the South China active continental margin.

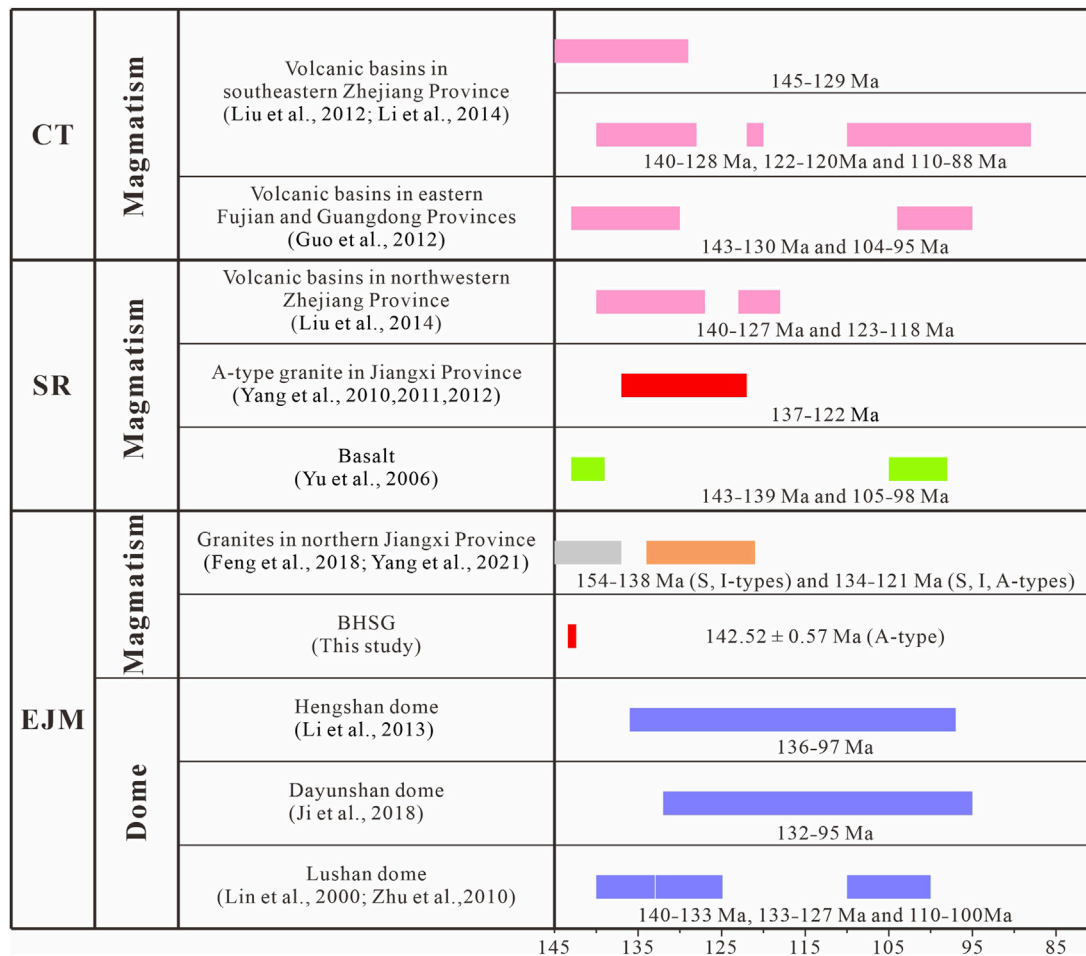


FIGURE 15

Diagram comparing the duration of extension-related geological records in different terranes of the SCB. Abbreviations: CT, coastal terrane, SR, Shi-Hang Rift, EJM, eastern Jiangnan Massif.

6 Conclusion

Baihesi granite is a highly evolved aluminous A-type granite with a concordant age of 142.52 ± 0.57 Ma (MSWD = 1.2), indicating the onset of the Cretaceous extension in the eastern Jiangnan Massif to be *ca.* 145–140 Ma.

The $\epsilon_{\text{Hf}}(t)$ values of Baihesi granite range from -5.57 to -2.37 , suggesting Baihesi granite originated mainly from partial melting of a reworked juvenile crust related to Neoproterozoic arc-related magmatism.

The formation of Baihesi granite was controlled by the subduction process along the South China active continental margin.

Data availability statement

The original contributions presented in the study are included in the article/Supplementary Material; further inquiries can be directed to the corresponding author.

Author contributions

Conceptualization, BH and DZ; methodology, BH; software, BH; validation, DZ and BH; formal analysis, BH; investigation, BH, DZ, and XZ; resources, DZ; data curation, BH; writing—original draft preparation, BH and DZ; writing—review and editing, DZ, ZZ, SW, and JH; visualization, BH; supervision, DZ; project administration, DZ; funding acquisition, DZ. All authors have read and agreed to the published version of the manuscript.

Funding

This research was funded by National Natural Science Foundation of China (Number 41772069), and the Geological Survey Achievement Transformation Fund of China University of Geosciences (Beijing).

Acknowledgments

The authors thank the editor and the reviewers for the constructive comments and thank Wuhan Sample Solution Analytical Technology Co., Ltd. for their help in the experimental analysis.

Conflict of interest

The authors declare that the research was conducted in the absence of any commercial or financial relationships that could be construed as a potential conflict of interest.

References

- Ballouard, C., Boulvais, P., Poujol, M., Gapais, D., Yamato, P., Tartese, R., et al. (2015). Tectonic record, magmatic history and hydrothermal alteration in the Hercynian Guerande leucogranite, Armorican Massif, France. *Lithos* 220, 1–22. doi:10.1016/j.lithos.2015.01.027
- Ballouard, C., Branquet, Y., Tartese, R., Poujol, M., Boulvais, P., and Vigneresse, J. L. (2016). Nb-Ta fractionation in peraluminous granites: A marker of the magmatic-hydrothermal transition. *Geology* 44, 231–234. doi:10.1130/g37475.1
- Bau, M. (1996). Controls on the fractionation of isovalent trace elements in magmatic and aqueous systems: Evidence from Y/Ho, Zr/Hf, and lanthanide tetrad effect. *Contributions Mineralogy Petrology* 123, 323–333. doi:10.1007/s004100050159
- Bonin, B. (2007). A-type granites and related rocks: Evolution of a concept, problems and prospects. *Lithos* 97, 1–29. doi:10.1016/j.lithos.2006.12.007
- Chappell, B. W., and White, A. J. R. (1992). I- and S-type granites in the lachlan fold belt. *Trans. R. Soc. Edinb. Earth Sci.* 83, 1–26. doi:10.1017/s0263593300007720
- Charvet, J. (2013). The neoproterozoic–early paleozoic tectonic evolution of the South China block: An overview. *J. Asian Earth Sci.* 74, 198–209. doi:10.1016/j.jseas.2013.02.015
- Chen, W., Chen, B., and Sun, K. (2018). Petrogenesis of the Maogongdong highly differentiated granite in the Dahutang tungsten ore field, Jiangxi Province. *Acta Petrol. Sin.* 34, 1704–1724. (In Chinese with English abstract).
- Chu, Y., Lin, W., Faure, M., and Wang, Q. (2015). Early mesozoic intracontinental orogeny: Example of the xuefengshan–jiuling belt. *Acta Petrol. Sin.* 31, 2145–2155. (In Chinese with English abstract).
- Chu, Y., Lin, W., Faure, M., Xue, Z., Ji, W., and Feng, Z. (2019). Cretaceous episodic extension in the South China block, east asia: Evidence from the yuechengling massif of central south China. *TECTONICS* 38, 3675–3702. doi:10.1029/2019tc005516
- Chu, Y., and Lin, W. (2014). Phanerozoic polyorogenic deformation in southern Jiuling Massif, northern South China block: Constraints from structural analysis and geochronology. *J. Asian Earth Sci.* 86, 117–130. doi:10.1016/j.jseas.2013.05.019
- Collins, W. J., Beams, S. D., White, A. J. R., and Chappell, B. W. (1982). Nature and origin of A-type granites with particular reference to southeastern Australia. *Contributions Mineralogy Petrology* 80, 189–200. doi:10.1007/bf00374895
- Dai, P., Mao, J., Wu, S., Xie, G., and Luo, X. (2018). Multiple dating and tectonic setting of the early cretaceous xianglushan W deposit, Jiangxi province, south China. *Ore Geol. Rev.* 95, 1161–1178. doi:10.1016/j.oregeorev.2017.11.017
- Dostal, J., Kontak, D. J., Gerel, O., Shellnutt, J. G., and Fayek, M. (2015). Cretaceous ongonites (topaz-bearing albite-rich microleucogranites) from ongon khairkhan, Central Mongolia: Products of extreme magmatic fractionation and pervasive metasomatic fluid: Rock interaction. *Lithos* 236, 173–189. doi:10.1016/j.lithos.2015.08.003
- Eby, G. N. (1992). Chemical subdivision of the A-type granitoids: Petrogenetic and tectonic implications. *Geology* 20, 641–644. doi:10.1130/0091-7613(1992)020<0641:csotat>2.3.co;2
- Eby, G. N., and Kochhar, N. (1990). Geochemistry and petrogenesis of the Malani igneous suite, north Peninsular India. *J. Geol. Soc. INDIA* 36, 109–130.
- Faure, M., Sun, Y., Shu, L., Monie, P., and Charvet, J. (1996). Extensional tectonics within a subduction-type orogen. The case study of the Wugongshan dome (Jiangxi Province, southeastern China). *TECTONOPHYSICS* 263, 77–106. doi:10.1016/s0040-1951(97)81487-4
- Feng, C., Wang, H., Xiang, X., and Zhang, M. (2018). Late mesozoic granite-related W-Sn mineralization in the northern Jiangxi region, se China: A review. *J. Geochem. Explor.* 195, 31–48. doi:10.1016/j.gexplo.2018.06.008
- Gan, C., Zhang, Y., Wang, Y., Qian, X., and Wang, Y. (2021). Reappraisal of the mesozoic tectonic transition from the paleo-tethyan to paleo-pacific domains in South China. *Geol. Soc. Am. Bull.* 133, 2582–2590. doi:10.1130/b35755.1

Publisher's note

All claims expressed in this article are solely those of the authors and do not necessarily represent those of their affiliated organizations, or those of the publisher, the editors, and the reviewers. Any product that may be evaluated in this article, or claim that may be made by its manufacturer, is not guaranteed or endorsed by the publisher.

Supplementary material

The Supplementary Material for this article can be found online at: <https://www.frontiersin.org/articles/10.3389/feart.2023.1085767/full#supplementary-material>

- Gelman, S. E., Deering, C. D., Bachmann, O., Huber, C., and Gutierrez, F. J. (2014). Identifying the crystal graveyards remaining after large silicic eruptions. *Earth Planet. Sci. Lett.* 403, 299–306. doi:10.1016/j.epsl.2014.07.005
- Gilder, S. A., Gill, J., Coe, R. S., Zhao, X. X., Liu, Z. W., Wang, G. X., et al. (1996). Isotopic and paleomagnetic constraints on the Mesozoic tectonic evolution of south China. *J. Geophys. RESEARCH-SOLID EARTH* 101, 16137–16154. doi:10.1029/96jb00662
- Goldschmidt, V. M. (1937). The principles of distribution of chemical elements in minerals and rocks: The seventh Hugo Müller Lecture delivered before the Chemical Society on March 17th, 1937. *J. Chem. Soc.*, 655–673. doi:10.1039/JR9370000655
- Guo, F., Fan, W., Li, C., Zhao, L., Li, H., and Yang, J. (2012). Multi-stage crust-mantle interaction in SE China: Temporal, thermal and compositional constraints from the Mesozoic felsic volcanic rocks in eastern Guangdong-Fujian provinces. *Lithos* 150, 62–84. doi:10.1016/j.lithos.2011.12.009
- He, X., Zhang, D., Di, Y., Wu, G., Hu, B., Huo, H., et al. (2022). Evolution of the magmatic-hydrothermal system and formation of the giant Zhuxi W-Cu deposit in South China. *Geosci. Front.* 13, 101278. doi:10.1016/j.gsf.2021.101278
- Hoskin, P. W. O. (2005). Trace-element composition of hydrothermal zircon and the alteration of Hadean zircon from the Jack Hills, Australia. *Geochimica Cosmochimica Acta* 69, 637–648. doi:10.1016/j.gca.2004.07.006
- Hu, Z. H., Lou, F. S., Li, Y. M., Li, J. M., Wang, X. G., Chen, J. P., et al. (2018). Geochemistry and petrogenesis of ore-related granite in the dongping tungsten deposit in wuning county, Jiangxi province. *Earth Sci.* 43, 243–263. (In Chinese with English abstract).
- Huang, L.-C., and Jiang, S.-Y. (2014). Highly fractionated S-type granites from the giant dahutang tungsten deposit in jiangnan orogen, southeast China: Geochronology, petrogenesis and their relationship with W-mineralization. *Lithos* 202, 207–226. doi:10.1016/j.lithos.2014.05.030
- Jackson, S. E., Pearson, N. J., Griffin, W. L., and Belousova, E. A. (2004). The application of laser ablation-inductively coupled plasma-mass spectrometry to *in situ* U-Pb zircon geochronology. *Chem. Geol.* 211, 47–69. doi:10.1016/j.chemgeo.2004.06.017
- Ji, W., Chen, Y., Chen, K., Wei, W., Faure, M., and Lin, W. (2018b). Multiple emplacement and exhumation history of the late mesozoic dayunshan-mufushan batholith in southeast China and its tectonic significance: 2. Magnetic fabrics and gravity survey. *J. Geophys. RESEARCH-SOLID EARTH* 123, 711–731. doi:10.1002/2017jb014598
- Ji, W., Faure, M., Lin, W., Chen, Y., Chu, Y., and Xue, Z. (2018a). Multiple emplacement and exhumation history of the late mesozoic dayunshan-mufushan batholith in southeast China and its tectonic significance: 1. Structural analysis and geochronological constraints. *J. Geophys. RESEARCH-SOLID EARTH* 123, 689–710. doi:10.1002/2017jb014597
- Jiang, Y.-H., Wang, G.-C., Liu, Z., Ni, C.-Y., Qing, L., and Zhang, Q. (2015). Repeated slab advance-retreat of the Palaeo-Pacific plate underneath SE China. *Int. Geol. Rev.* 57, 472–491. doi:10.1080/00206814.2015.1017775
- Jiang, Y.-H., Zhao, P., Zhou, Q., Liao, S.-Y., and Jin, G.-D. (2011). Petrogenesis and tectonic implications of Early Cretaceous S- and A-type granites in the northwest of the Gan-Hang rift, SE China. *Lithos* 121, 55–73. doi:10.1016/j.lithos.2010.10.001
- King, P. L., Chappell, B. W., Allen, C. M., and White, A. J. R. (2001). Are A-type granites the high-temperature felsic granites? Evidence from fractionated granites of the wangrahs suite. *Aust. J. EARTH Sci.* 48, 501–514. doi:10.1046/j.1440-0952.2001.00881.x
- King, P. L., White, A. J. R., Chappell, B. W., and Allen, C. M. (1997). Characterization and origin of aluminous A-type granites from the lachlan fold belt, southeastern Australia. *J. Petrology* 38, 371–391. doi:10.1093/ptroj/38.3.371
- Large, R. R., Gemmill, J. B., Paulick, H., and Huston, D. L. (2001). The alteration box plot: A simple approach to understanding the relationship between alteration mineralogy

- and litho geochemistry associated with volcanic-hosted massive sulfide deposits. *Econ. Geol.* 96, 957–971. doi:10.2113/96.5.957
- Laurent, O., Björnsen, J., Wotzlaw, J.-F., Bretscher, S., Pimenta Silva, M., Moyen, J.-F., et al. (2020). Earth's earliest granitoids are crystal-rich magma reservoirs tapped by silicic eruptions. *Nat. Geosci.* 13, 163–169. doi:10.1038/s41561-019-0520-6
- Lechler, P. J., and Desilets, M. O. (1987). A review of the use of loss on ignition as a measurement of total volatiles in whole-rock analysis. *Chem. Geol.* 63, 341–344. doi:10.1016/0009-2541(87)90171-9
- Li, C., Wang, Z., Lu, Q., Tan, Y., Li, L., Tao, T., et al. (2021). Mesozoic tectonic evolution of the eastern South China Block: A review on the synthesis of the regional deformation and magmatism. *Ore Geol. Rev.* 131. doi:10.1016/j.oregeorev.2021.104028
- Li, C., Wang, Z., Wang, D., Cao, W., Yu, X., Zhou, G., et al. (2014). Crust-mantle interaction triggered by oblique subduction of the Pacific plate: geochronological, geochemical, and Hf isotopic evidence from the Early Cretaceous volcanic rocks of Zhejiang Province, southeast China. *Int. Geol. Rev.* 1756, 1732–1753. doi:10.1080/00206814.2014.956347
- Li, J., Dong, S., Gao, R., Cawood, P. A., Zhang, Y., Zhao, G., et al. (2022). New insights into Phanerozoic tectonics of South China: Part 1, polyphase deformation in the jiuiling and lianyunshan domains of the central jiangnan orogen. *Tect. Geophys. Res. Solid Earth* 41121, 3048–3080. doi:10.1002/2015jb012778
- Li, J., Dong, S., Zhang, Y., Zhao, G., Johnston, S. T., Cui, J., et al. (2016). New insights into Phanerozoic tectonics of south China: Part 1, polyphase deformation in the Jiuiling and Lianyunshan domains of the central Jiangnan Orogen. *J. Geophys. Res. Solid Earth* 121, 3048–3080. doi:10.1002/2015JB012778
- Li, J., Zhang, Y., Dong, S., and Johnston, S. T. (2014). Cretaceous tectonic evolution of South China: A preliminary synthesis. *EARTH-SCIENCE Rev.* 134, 98–136. doi:10.1016/j.earscirev.2014.03.008
- Li, J., Zhang, Y., Dong, S., Su, J., Li, Y., Cui, J., et al. (2013). The Hengshan low-angle normal fault zone: Structural and geochronological constraints on the Late Mesozoic crustal extension in South China. *TECTONOPHYSICS* 606, 97–115. doi:10.1016/j.tecto.2013.05.013
- Li, X.-H., Li, W.-X., Li, Z.-X., Lo, C.-H., Wang, J., Ye, M.-F., et al. (2009). Amalgamation between the Yangtze and Cathaysia blocks in South China: Constraints from SHRIMP U-Pb zircon ages, geochemistry and Nd-Hf isotopes of the shuangxiwu volcanic rocks. *Precambrian Res.* 174, 117–128. doi:10.1016/j.precamres.2009.07.004
- Li, X., Long, W., Li, Q., Liu, Y., Zheng, Y., Yang, Y., et al. (2010). Penglai zircon megacrysts: A potential new working reference material for microbeam determination of Hf-O isotopes and U-Pb age. *Geostand. GEOANALYTICAL Res.* 34, 117–134. doi:10.1111/j.1751-908x.2010.00036.x
- Li, Z.-X., and Li, X.-H. (2007). formation of the 1300-km-wide intracontinental orogen and postorogenic magmatic province in mesozoic south China: A flat-slab subduction model. *Geology* 35, 179–182. doi:10.1130/g23193a.1
- Lin, W., Faure, M., Monie, P., Scharer, U., Zhang, L. S., and Sun, Y. (2000). Tectonics of SE China: New insights from the lushan massif (jiangxi province). *TECTONICS* 19, 852–871. doi:10.1029/2000tc900009
- Liu, J. L., Ni, J. L., Chen, X. Y., Craddock, J. P., Zheng, Y. Y., Ji, L., et al. (2021). Cretaceous Pacific plate movement beneath SE China: Evidence from episodic volcanism and related intrusions. *EARTH-SCIENCE Rev.* 217614, 170–184. doi:10.1016/j.tecto.2013.12.007
- Liu, L., Xu, X., and Xia, Y. (2014). Cretaceous Pacific plate movement beneath SE China: Evidence from episodic volcanism and related intrusions. *TECTONOPHYSICS* 614, 170–184. doi:10.1016/j.tecto.2013.12.007
- Liu, L., Xu, X., and Zou, H. (2012). Episodic eruptions of the Late Mesozoic volcanic sequences in southeastern Zhejiang, SE China: Petrogenesis and implications for the geodynamics of paleo-Pacific subduction. *Lithos* 154, 166–180. doi:10.1016/j.lithos.2012.07.002
- Liu, P., Mao, J., Santosh, M., Bao, Z., Zeng, X., and Jia, L. (2018). Geochronology and petrogenesis of the Early Cretaceous A-type granite from the Feie'Shan W-Sn deposit in the eastern Guangdong Province, SE China: Implications for W-Sn mineralization and geodynamic setting. *Lithos* 300, 330–347. doi:10.1016/j.lithos.2017.12.015
- Liu, Y., Gao, S., Hu, Z., Gao, C., Zong, K., and Wang, D. (2010). Continental and oceanic crust recycling-induced melt-peridotite interactions in the trans-north China orogen: U-Pb dating, Hf isotopes and trace elements in zircons from mantle xenoliths. *J. Petrology* 51, 537–571. doi:10.1093/ptrology/egp082
- Loiselle, M. C., and Wones, D. R. (1979). *Characteristics and origin of anorogenic granites*, 11. San Diego, CA: Geological Society of America Abstracts with Programs, 468.
- Lou, F., Shen, W., Wang, D., Shu, L., Wu, F., Zhang, F., et al. (2005). Zircon U-Pb isotopic chronology of the wugongshan dome compound granite in Jiangxi province. *ACTA Geol. SIN.* 79, 636–644. (In Chinese with English abstract).
- Luo, L., Jiang, S. Y., Yang, S. Y., and Zhao, K. D. Petrochemistry (2010). Zircon U-Pb dating and Hf isotopic composition of the granitic pluton in the Pengshan Sn-polymetallic orefield, Jiangxi Province. *Acta Petrol. Sin.* 26, 2818–2834. (In Chinese with English abstract).
- MacLean, W. H. (1990). Mass change calculations in altered rock series. *Miner. Deposita* 25, 44–49. doi:10.1007/bf03326382
- Maniar, P. D., and Piccoli, P. M. (1989). Tectonic discrimination of granitoids. *Geol. Soc. Am. Bull.* 101, 635–643. doi:10.1130/0016-7606(1989)101<0635:tdog>2.3.co;2
- Mao, J., Xiong, B., Liu, J., Pirajno, F., Cheng, Y., Ye, H., et al. (2017). Molybdenite Re/Os dating, zircon U-Pb age and geochemistry of granitoids in the Yangchuling porphyry W-Mo deposit (Jiangnan tungsten ore belt), China: Implications for petrogenesis, mineralization and geodynamic setting. *Lithos* 286, 35–52. doi:10.1016/j.lithos.2017.05.023
- Middlemost, E. A. K. (1994). Naming materials in the magma/igneous rock system. *EARTH-SCIENCE Rev.* 37, 215–224. doi:10.1016/0012-8252(94)90029-9
- Miller, C. F., and Mittlefehldt, D. W. (1982). Depletion of light rare-earth elements in felsic magmas. *Geology* 10, 129–133. doi:10.1130/0091-7613(1982)10<129:dolrei>2.0.co;2
- Miller, C. F., and Mittlefehldt, D. W. (1984). Extreme fractionation in felsic magma chambers: A product of liquid-state diffusion or fractional crystallization? *Earth Planet. Sci. Lett.* 68, 151–158. doi:10.1016/0012-821x(84)90147-x
- Mo, X. (2019). Magmatism and deep geological process. *Earth Sci.* 44, 1487–1493. (In Chinese with English abstract).
- Pan, F.-B., Liu, R., Jin, C., Jia, B.-J., He, X., Gao, Z., et al. (2018). Petrogenesis of early cretaceous granitoids from southwest Zhejiang, NE south China block and its geodynamic implication. *Lithos* 308, 196–212. doi:10.1016/j.lithos.2018.03.011
- Pan, X., Hou, Z., Zhao, M., Chen, G., Rao, J., Li, Y., et al. (2018). Geochronology and geochemistry of the granites from the Zhuxi W-Cu ore deposit in South China: Implication for petrogenesis, geodynamical setting and mineralization. *Lithos* 304, 155–179. doi:10.1016/j.lithos.2018.01.014
- Pearce, J. A., Harris, N. B. W., and Tindle, A. G. (1984). Trace element discrimination diagrams for the tectonic interpretation of granitic rocks. *J. Petrology* 25, 956–983. doi:10.1093/ptrology/25.4.956
- Peccerillo, A., and Taylor, S. R. (1976). Geochemistry of eocene calc-alkaline volcanic rocks from the Kastamonu area, Northern Turkey. *Contributions Mineralogy Petrology* 58, 63–81. doi:10.1007/bf00384745
- Qiu, J.-T., and Qiu, L. (2016). Geochronology and magma oxygen fugacity of Ehu S-type granitic pluton in Zhe-Gan-Wan region, SE China. *Chem. DER ERDE-GEOCHEMISTRY* 76, 441–448. doi:10.1016/j.chemer.2016.06.004
- Rogers, J. J. W., and Greenberg, J. K. (1990). Late-orogenic, post-orogenic, and anorogenic granites: Distinction by major-element and trace-element chemistry and possible origins. *J. Geol.* 98, 291–309. doi:10.1086/629406
- Shu, L. (2021). Principal features of intracontinental orogenic belt and discussions on its dynamics. *ACTA Geol. SIN.* 95, 98–106. (In Chinese with English abstract).
- Shu, L. S., Zhou, G. Q., Shi, Y. S., and Yin, J. (1994). Study of the high pressure metamorphic blueschist and its late proterozoic age in the eastern jiangnan belt. *Chin. Sci. Bull.* 39, 1200–1204.
- Shu, L. S., Zhou, X. M., Deng, P., Wang, B., Jiang, S. Y., Yu, J. H., et al. (2009). Mesozoic tectonic evolution of the Southeast China Block: New insights from basin analysis. *J. Asian Earth Sci.* 34, 376–391. doi:10.1016/j.jseas.2008.06.004
- Sláma, J., Košler, J., Condon, D. J., Crowley, J. L., Gerdes, A., Hanchar, J. M., et al. (2008). Plešovice zircon — a new natural reference material for U–Pb and Hf isotopic microanalysis. *Chem. Geol.* 249, 1–35. doi:10.1016/j.chemgeo.2007.11.005
- Smith, R. E., and Smith, S. E. (1976). Comments on the use of Ti, Zr, Y, Sr, K, P and Nb in classification of basaltic magmas. *Earth Planet. Sci. Lett.* 32 (2), 114–120. doi:10.1016/0012-821x(76)90049-2
- Streckeisen, A., and Le Maitre, R. W. (1979). A chemical approximation to the modal QAPF classification of the igneous rocks. *Neues Jahrb. für Mineral. Abh.* 136, 169–206.
- Sun, H., Li, J., Zhang, Y., Dong, S., Xin, Y., and Yu, Y. (2018). Early Paleozoic tectonic reactivation of the Shaoxing-Jiangshan fault zone: Structural and geochronological constraints from the Chencai domain, South China. *J. Struct. Geol.* 110, 116–130. doi:10.1016/j.jsg.2018.03.003
- Sun, S. s., and McDonough, W. F. (1989). Chemical and isotopic systematics of oceanic basalts: Implications for mantle composition and processes. *Geol. Soc. Lond. Spec. Publ.* 42, 313–345. doi:10.1144/gsl.sp.1989.042.01.19
- Suo, Y., Li, S., Jin, C., Zhang, Y., Zhou, J., Li, X., et al. (2019). Eastward tectonic migration and transition of the Jurassic-Cretaceous Andean-type continental margin along Southeast China. *EARTH-SCIENCE Rev.* 196, 102884. doi:10.1016/j.earscirev.2019.102884
- Sylvester, P. J. (1989). Post-collisional alkaline granites. *J. Geol.* 97, 261–280. doi:10.1086/629302
- Vermeesch, P. IsoplotR. (2018). IsoplotR: A free and open toolbox for geochronology. *Geosci. Front.* 9, 1479–1493. doi:10.1016/j.gsf.2018.04.001
- Wang, D., Wang, X.-L., Zhou, J.-C., and Shu, X.-J. (2013). Unraveling the precambrian crustal evolution by neoproterozoic conglomerates, jiangnan orogen: U–Pb and Hf isotopes of detrital zircons. *Precambrian Res.* 233, 223–236. doi:10.1016/j.precamres.2013.05.005
- Wang, F., Chen, H., Batt, G. E., Lin, X., Gong, J., Gong, G., et al. (2015). Tectonothermal history of the NE Jiangshan-Shaoxing suture zone: Evidence from 40Ar/39Ar and fission-track thermochronology in the Chencai region. *Precambrian Res.* 264, 192–203. doi:10.1016/j.precamres.2015.04.009
- Wang, J.-l., He, B., and Guan, J.-p. (2013). Study on age and mechanism of the metamorphism of the xingzi group in the lushan area, Jiangxi province. *Geotect. Metallogenia* 37, 489–498.
- Wang, L.-j., Zhang, K.-x., Lin, S.-f., He, W.-h., and Yin, L.-m. (2022). Origin and age of the shenshan tectonic melange in the jiangshan-shaoxing-pingxiang fault and late early paleozoic juxtaposition of the Yangtze block and the west Cathaysia terrane, south China. *Geol. Soc. Am. Bull.* 134, 113–129. doi:10.1130/b35963.1

- Wang, X.-L., Zhao, G., Zhou, J.-C., Liu, Y., and Hu, J. (2008). Geochronology and Hf isotopes of zircon from volcanic rocks of the Shuangqiaoshan Group, South China: Implications for the Neoproterozoic tectonic evolution of the eastern Jiangnan orogen. *Gondwana Res.* 14, 355–367. doi:10.1016/j.gr.2008.03.001
- Wang, X.-L., Zhou, J.-C., Griffin, W. L., Zhao, G., Yu, J.-H., Qiu, J.-S., et al. (2014). Geochemical zonation across a Neoproterozoic orogenic belt: Isotopic evidence from granitoids and metasedimentary rocks of the Jiangnan orogen, China. *Precambrian Res.* 242, 154–171. doi:10.1016/j.precamres.2013.12.023
- Watson, E. B., and Harrison, T. M. (1983). Zircon saturation revisited: Temperature and composition effects in a variety of crustal magma types. *Earth Planet. Sci. Lett.* 64, 295–304. doi:10.1016/0012-821x(83)90211-x
- Whalen, J. B., Currie, K. L., and Chappell, B. W. (1987). A-Type granites: Geochemical characteristics, discrimination and petrogenesis. *Contributions Mineralogy Petrology* 95, 407–419. doi:10.1007/bf00402202
- Wong, J., Sun, M., Xing, G. F., Li, X. H., Zhao, G. C., Wong, K., et al. (2009). Geochemical and zircon U-Pb and Hf isotopic study of the Baijhuajian metaluminous A-type granite: Extension at 125–100 Ma and its tectonic significance for South China. *Lithos* 112, 289–305. doi:10.1016/j.lithos.2009.03.009
- Wu, F., Liu, X., Ji, W., Wang, J., and Yang, L. (2017). Highly fractionated granites: Recognition and research. *Sci. China-Earth Sci.* 60, 1201–1219. doi:10.1007/s11430-016-5139-1
- Xu, Q., Liu, S., Wang, Z., and Zhang, B. (2019). Provenance of the East Guangdong Basin and Yong'an Basin in southeast China: Response to the Mesozoic tectonic regime transformation. *J. Asian Earth Sci.*, 18. doi:10.1016/j.jseas.2019.104024
- Yang, S.-Y., Jiang, S.-Y., Jiang, Y.-H., Zhao, K.-D., and Fan, H.-H. (2011). Geochemical, zircon U-Pb dating and Sr-Nd-Hf isotopic constraints on the age and petrogenesis of an Early Cretaceous volcanic-intrusive complex at Xiangshan, Southeast China. *MINERALOGY PETROLOGY* 101, 21–48. doi:10.1007/s00710-010-0136-4
- Yang, S.-Y., Jiang, S.-Y., Zhao, K.-D., Jiang, Y.-H., Ling, H.-F., and Luo, L. (2012). Geochronology, geochemistry and tectonic significance of two Early Cretaceous A-type granites in the Gan-Hang Belt, Southeast China. *Lithos* 150, 155–170. doi:10.1016/j.lithos.2012.01.028
- Yang, Y. S., Pan, X. F., Hou, Z. Q., and Deng, Y. (2021). Redox states and protoliths of late mesozoic granitoids in the eastern jiangnan orogen: Implications for W, Mo, Cu, Sn, and (Au) mineralization. *Ore Geol. Rev.* 134.
- Yao, J., Cawood, P. A., Shu, L., and Zhao, G. (2019). Jiangnan orogen, south China: A ~970–820 Ma rodinia margin accretionary belt. *EARTH-SCIENCE Rev.* 196, 102872.
- Yao, J., Shu, L., Santosh, M., and Li, J. (2012). Precambrian crustal evolution of the South China Block and its relation to supercontinent history: Constraints from U-Pb ages, Lu-Hf isotopes and REE geochemistry of zircons from sandstones and granodiorite. *Precambrian Res.* 208, 19–48. doi:10.1016/j.precamres.2012.03.009
- Ye, M.-F., Li, X.-H., Li, W.-X., Liu, Y., and Li, Z.-X. (2007). SHRIMP zircon U-Pb geochronological and whole-rock geochemical evidence for an early Neoproterozoic Sibaoan magmatic arc along the southeastern margin of the Yangtze Block. *Gondwana Res.* 12, 144–156. doi:10.1016/j.gr.2006.09.001
- Yu, X., Wu, G., Zhang, D., Yan, T., Di, Y., and Wang, L. (2006). Cretaceous extension of the ganhang tectonic belt, southeastern China: Constraints from geochemistry of volcanic rocks. *Cretac. Res.* 27, 663–672. doi:10.1016/j.cretres.2006.03.008
- Zhang, Y., Xu, X., Jia, D., and Shu, L. (2009). Deformation record of the change from Indosinian collision-related tectonic system to Yanshanian subduction-related tectonic system in South China during the Early Mesozoic. *Earth Sci. Front.* 16, 234–247. (In Chinese with English abstract).
- Zhang, Z., Hu, B., Zhang, D., He, X., Zou, J., Tian, X., et al. (2022). *Genesis and significance of late cretaceous granitic magmatism in xianghualing tin-polymetallic orefield, nanling region, South China*. Basel, Switzerland: APPLIED SCIENCES-BASEL, 12. doi:10.3390/app12188984
- Zhang, Z., Hu, B., Zhang, D., Xiong, G., Zhu, X., Jia, W., et al. (2020). Zircon U-Pb age, geochemistry and Hf isotope characteristics of Shimensi granite porphyry in northern Jiangxi Province and its constraint on mineralization. *Geol. Bull. China* 39, 1267–1284. (In Chinese with English abstract).
- Zhao, G., and Cawood, P. A. (2012). Precambrian geology of China. *Precambrian Res.* 222–223, 13–54. doi:10.1016/j.precamres.2012.09.017
- Zhou, X. M., and Li, W. X. (2000). Origin of Late Mesozoic igneous rocks in Southeastern China: Implications for lithosphere subduction and underplating of mafic magmas. *TECTONOPHYSICS* 326, 269–287. doi:10.1016/s0040-1951(00)00120-7
- Zhou, X. M., Sun, T., Shen, W. Z., Shu, L. S., and Niu, Y. L. (2006). Petrogenesis of mesozoic granitoids and volcanic rocks in South China: A response to tectonic evolution. *Episodes* 29, 26–33. doi:10.18814/epiugs/2006/v29i1/004
- Zhu, Q., Yang, K., and Wang, Y. (2010). Extensional detachment and magmatism of the lushan metamorphic core complex: Constraints from $^{40}\text{Ar}/^{39}\text{Ar}$ and U-Pb geochronology. *Geotect. Metallogenia* 34, 391–401.
- Zong, K., Klemd, R., Yuan, Y., He, Z., Guo, J., Shi, X., et al. (2017). The assembly of Rodinia: The correlation of early Neoproterozoic (ca. 900 Ma) high-grade metamorphism and continental arc formation in the southern Beishan Orogen, southern Central Asian Orogenic Belt (CAOB). *Precambrian Res.* 290, 32–48. doi:10.1016/j.precamres.2016.12.010